Technische Universität München

A silicon tracker system for (p,2p) reactions

MASTER'S THESIS by LUKAS WERNER

LEHRSTUHL ENA FÜR EXPERIMENTALPHYSIK

THURSDAY 13TH OCTOBER, 2016

Master's thesis by Lukas Werner

A silicon tracker for (p,2p) reactions

Ein Siliziumdetektorsystem für (p,2p) Reaktionen

Technical University Munich
Faculty for Physics

Chair ENA for
Experimental Nuclear Astrophysics

RIKEN Nishina Center for Accelerator-Based Science

AUTHOR: Lukas Werner

SUPERVISOR: Prof. Dr. Shawn Bishop

ADVISOR: Dr. Roman Gernhäuser

Abstract

The observations of elemental and isotopic abundances in different sites of our universe are major input to our understanding of astrophysics. This concerns all stages in time from the big bang to the present and in scales from small very old stars of the first generations up to the dynamics in galaxy clusters and superclusters. Currently the most successful models confirm the major contributions of the r-process, especially for the abundance patterns of heavy nuclei above the magic nuclear shell of N, Z =50. These models predict a strong influence of fission barrier heights on the distribution of r-process nuclei, mainly through termination of the r-process via neutron induced fission of heavier nuclei, and simultaneously by a recycling of the fission products, refueling the r-process with neutron rich, lower mass nuclei. Contrary to this important influence of the fission on the r-process, experimental data on fission barriers is scarce, especially for neutron rich, exotic nuclei. A new experimental approach to investigate fission barriers is the quasi-free scattering process (p, 2p) in inverse kinematics. Using a relativistic heavy ion beam and a liquid hydrogen target will allow for a precise determination of barrier heights for even the most unstable nuclei. Excitation energies can be determined precisely by a kinematically complete measurement of the outgoing particles.

For this purpose a silicon tracker system has been developed, using highly segmented, thin (23 mg/cm^2) silicon detectors, with a low noise readout (σ_{enc}<10 keV). Minimizing the angular straggling they still allow for a high tracking efficiency of 97.2% for both protons within the acceptance. The high quality electronics developed for the readout of the system was tested for trigger rates up to 80 kHz without introducing dead time.

The silicon tracker has been used in an experiment at the HIMAC facility in Japan, with a stable ^{16}O beam at energies of E=290 MeV/u. Specialized targets were developed, to allow for a precise study of the achievable position resolution. The target structure was reconstructed using a tracking algorithm also developed in the framework of this thesis. The resulting position resolution of Δ_x = 412 $\pm^{12}_{28}$ μm in FWHM is in very good agreement with expectations from extensive Geant4 simulations for the tracker, showing that the system works at its full capacity.

This first experiment suggests that the tracker developed here is well suited for its intended use at the RIKEN facility, together with the SAMURAI spectrometer. Several possible improvements of the setup for these experiments were also investigated. Tagged fiber and active fiber targets, would allow a superior position resolution for the system, but limit the maximum target thickness.

Contents

1 Study of fission barriers with the (p,2p) reaction 1
1.1 Nuclear abundances and the r-process 1
1.2 Fission 2
1.3 The (p,2p) reaction 3
1.4 RIBF 5

2 A detector setup for the (p,2p) reaction 9
2.1 Experimental concept 9
2.2 Simulation of detector response 11

3 Detector development 15
3.1 Silicon detectors 15
3.2 Analogue read out electronics 18
3.3 Digital read out electronics 20
3.4 Dead time free system integration 23

4 Experiment at HIMAC 25
4.1 The HIMAC facility 25
4.2 Detector setup 26

5 Data analysis 33
5.1 Particle identification and tracking 33
5.2 Vertex reconstruction 36
5.3 (p,2p) reaction 39
5.4 Efficiency 41

6 Summary and outlook 45
6.1 Further improvements of the setup 46

Bibliography 51

Chapter 1

Study of fission barriers with the (p,2p) reaction

1.1 Nuclear abundances and the r-process

The production of non primordial nuclei is believed to happen in several distinct processes. Light nuclei up to isotopes like ^{58}Ni can be produced by fusion. For heavier nuclei this is energetically not possible, since they have a lower binding energy. This is circumvented by the so called slow neutron capture, or s-process, where neutrons are added to an existing nuclei, which is believed to happen in the asymptotic giant branch of the Hertzsprung-Russel diagram. Because of the low neutron flux in this process, unstable nuclei produced will undergo β^- decay back to the valley of stability, thereby producing heavier elements. [1]

Roughly half of the nuclei with A>60 observed in the solar system were not produced with the s-process. A likely production process for this nuclei is the rapid neutron capture or r-process. In this process, a very high neutron flux allows for neutron capture in time scales below the half lives of most known nuclei. This allows for the production of heavy, very neutron rich nuclei. Very far away of stability an equilibrium between neutron capture and β-decay is reached to produce even the heaviest of isotopes. It is still unclear which astrophysical sites host the r-process, although type-II supernovae and neutron star mergers are likely candidates. [2],[3]

In the r-process very heavy nuclei can be produced. If a heavy nucleus is bombarded with a neutron, it may undergo fission. This would terminate the r-process, blocking it from reaching heavier nuclei. Currently experimental data for fission barrier heights of neutron rich heavy nuclei is rare, making predictions for the termination of the r-process difficult. If r-process nuclei undergo fission, it is reasonable to assume, that one, or both of the daughter nuclei produced would be neutron rich, while it is also likely that neutrons would be evaporated from the mother nucleus. This nuclei would also undergo neutron capture, while the evaporated neutrons would increase the neutron density in the production site. Together this means a recycling of the fragments of the mother nucleus back into the r-process, thereby heavily influencing the distribution of isotopes produced in the r-process. For this reasons nuclear fission plays an important role in understanding the nuclear abundances in our solar system. [4],[2],[3]

1.2 Fission

Even in a semiclassical picture fission is the successive deformation of a nucleus. That leads to a further deformation and the formation of two charge centres and the following separation of this two charge centres. For basic calculations, this can be viewed similar to the fission of a liquid drop into two smaller ones. [5], [6] The size and composition of the two most likely charge centres of a nucleus, as well as the height of the potential barrier between the ground state and the two daughter nuclei, the fission barrier height, are subjects of ongoing research. [7]

Two types of fission can be distinguished. Spontaneous fission takes place, when a nucleus, in the ground or an exited state, sits in a local potential minimum. It is now possible for this nucleus, to tunnel out of this minimum. If it thereby reaches an unstable configuration, it will undergo a decay, or fission, to reduce its potential energy. [8],[9] In an induced fission process, the passing over this potential barrier is forced by exiting the nucleus.

When a nucleus undergoes inelastic scattering, for example with an incoming proton, the resulting deformation can shift its potential level. The deformation of the nucleus will follow the path with the lowest potential maximum between the ground state and the final state of deformation, which can be, depending on the exitation energy, fission. [6],[7]

Therefore the calculation of barrier heights is not a straightforward task. First a phase space of possible deformations of nuclei has to be defined. Then a potential has to be computed for each of this shapes. After this, the potential paths of fission have to be examined, and the path with the lowest maximal potential height has to be chosen. [7]

For the calculation of the potentials several different models have been developed.[4] One approach is to distinguish between a macroscopic part of the potential, which is the potential of the nucleus calculated with a finite range droplet model, and a microscopic part, wherein corrections for shell effects, and nucleon-nucleon-paring for protons and neutrons are summed up. For a detailed description see [10].

This has been used by P.Möller et. al. to calculate fission barrier heights for super heavy and neutron rich nuclei. [7] From this, a main motivations for investigating fission processes can be derived, namely the study of the so called island of stability, a theoretically predicted region, marked by the high values for fission barriers (As can be seen in Fig. 33 of [7]), and long lived nuclei. [11],[12] To improve the understanding of this phenomenon, experimental input for fission barrier heights of nuclei as heavy as currently possible is needed.

Fission barrier heights have been studied with a variety of tools. One of them is the use of a (d,p) reaction, a neutron transfer reaction, as it is done e.g. at ISOLDE. In this approach, a low energy beam of exotic nuclei is shot on a deuterium target.[13] This experiments are difficult, because a slow beam of exotic nuclei may undergo decay before it reaches the target. Also, it might not be completely ionized, making a identification of the fission fragments using charge to mass ratios difficult. This can be circumvented by using a proton knock out reaction like the (p,2p) reaction. In this type of reaction there is no longer a necessity to have beam energies below the coulomb barrier of the nuclei, allowing for high energy beams.

1.3 The (p,2p) reaction

In the (p,2p) reaction, a incoming proton knocks out a proton bound in a target nucleus. This can take place if the incident nucleon has an energy of several hundred MeV. This process can lead either to a Z-1 daughter nucleus in the ground state or the nucleus gets exited. The spectrum of the excitation energy can then be used to investigate topics like nuclear structure [14], or, as is planned with the detector system presented here, to study fission barrier heights.

The (p,2p) reaction can be viewed as a quasi-free-scattering process. This is justified by the high energy of the incident proton, far above the binding energies of the protons of the target nucleus. [8] In higher order approximations of this process one has to consider also interactions with other nucleons. These interactions also allow for an excitation of the nucleus. [15]

One method to describe this transfer of energy from the incident proton onto the nucleus is the distorted wave impulse approximation (DWIA). This model assumes that most of the energy transfer in the (p,2p) reaction happens between the two protons, while the effects of multiple scattering of the incoming proton with the nucleons are taken into account with distorted waves, describing the interaction of the incident proton with the mean potential of the nucleus. Effectively, one seperates between an elastic scattering between the two protons, and an inelastic scattering between the incident proton and the nucleus. [15], [16]

If a nucleus is exited this way, one of three things can happen. If the excitation energy is low enough that no other nucleons get evaporated from the nucleus, and the nucleus does not fission or fragment, one can effectively do a spectroscopic analysis of this exited states. [8] If the excitation energy increases over the binding energy of the nucleons, evaporation of neutrons and protons becomes possible, and thereby a deexcitation of the nucleus happens. [17] If enough energy is deposited in the nucleus, and no evaporation of nuclei happens, fission or fragmentation of the nucleus become possible. The likelihood for fission processes compared to evaporation processes increases with the ratio of the binding energy of the nuclei and the fission barrier height. [18]

A measurement procedure designed to get the Q-value of the (p,2p)-reaction has to measure the four-momenta of all particles involved. The Q-value of the system is per definition:

$$Q^2 = (p_A - p_1 - p_2 - p_{A-1})^2 \tag{1.1}$$

with p_A the four-momentum of the incoming nucleus,p_{A-1} the four-momentum of the outgoing nucleus, and p_1 and p_2 the four-momenta of the two protons. Using conservation of momenta this simplifies to

$$Q^2 = (E_A + m_p - (E_1 + E_2 + E_{A-1}))^2 \tag{1.2}$$

with m_p the mass of the proton. E_{A-1} is the energy of the nucleus right after the reaction, which is experimentally not available, since the nucleus might still undergo de-excitation after the primary reaction. This can be circumvented by using four-momenta conservation. One arrives at the following expression:

$$E_{A-1} = \sqrt{m_{A-1}^2 + (\overrightarrow{p}_A - \overrightarrow{p}_1 - \overrightarrow{p}_2)^2} \tag{1.3}$$

Which consists only of experimentally accessible quantities. Therefore a measurement of the four-momenta of the incoming nucleus and the two outgoing protons is sufficient, to measure the Q-value of the reaction if the bound state mass of the residual nucleus is known. The experimental goal is to measure the probabilities of excitation reaction channels and their dependence on the exitation energy in the A-1 nucleus.

1.4 RIBF

If not stated otherwise, all information in section 1.4 will be taken from [19].

Projectile Fragmentation is currently the most efficient method for producing extremely neutron rich isotopes especially for the heavy mass region. In projectile fragmentation a relativistic stable beam is shot on a light target (for example Be) and thereby fragmented. The produced nuclei can than be separated by magnetic fields using also the element specific energy loss in so called fragment separators.

The structure of a production facility for heavy, neutron rich isotopes will be described here on the example of the radioactive isotope beam factory (RIBF) at Riken, Nishina Center.

For the production of high intensity stable primary beams, the RIBF uses a electron cyclotron resonance source (ECRIS) and a superconducting ECRIS as sources. In an ECRIS, a hot electron plasma is produced through microwaves and bottled in by a magnetic field. Using an electric field, ions can be extracted from the plasma. [20] This sources are used to feed a linear accelerator, which can provide ions up to 6 MeV/u. Ions with a mass-to-charge ratio smaller then 4, can alternatively be injected into a cyclotron and be accelerated to a maximum energy of 14.5 MeV/u. After this, the ions are injected into the so called RRC, a ring cyclotron with K=540 MeV.

Following this, ions can be injected into the fRC, a room temperature, fixed frequency cyclotron with a frequency of 55 MHz and K=570 MeV. The fRC is followed by a ring cyclotron with a K-value of 970 MeV named IRC which can be fed by ether the RRC or the fRC. It yields a maximum energy of 127 MeV/u. Downstream of the IRC a superconducting ring cyclotron (SRC) is placed. This accelerator can ejected for example uranium ions of 345 MeV/u.

The primary beam is then guided onto a production target. Typically used beams are ^{48}Ca, ^{86}Kr, ^{136}Xe and ^{238}U. The resulting Isotopes and there intensities can be seen in Fig.1.1. The produced isotopes cover a large area of the chart of nuclei, and even regions of very exotic nuclei have significant production yields.

The reaction products of the fragmentation reactions, but also in case of coulomb induced fission, are very much forward focussed, covering only a rather narrow space in momentum around the beam. This secondary beam also possesses a large number of different isotopes. The beam has to be focussed, and an isotope

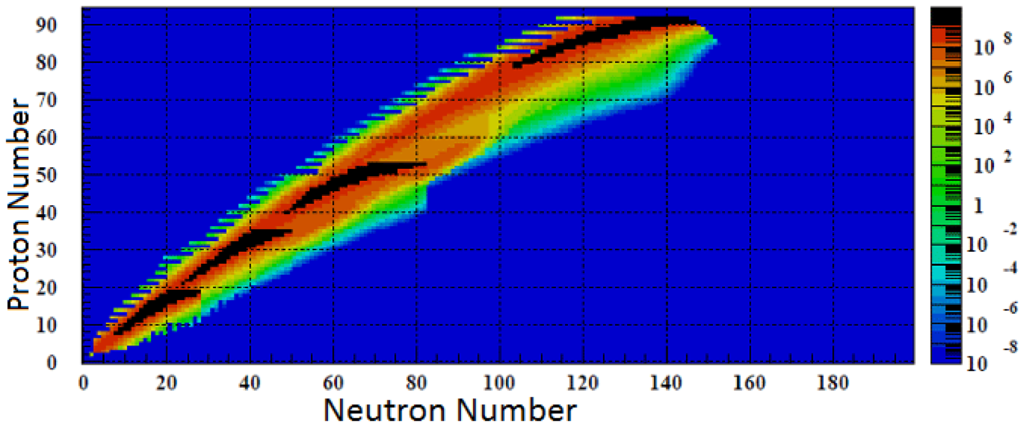

Figure 1.1: Production intensities for the RIBF, in particles per second (colour code on the right edge). If two beam-target combinations can produce the same isotope the higher intensity has been chosen. Taken from [21]

separation has to be performed. This is the purpose of the BigRIPS, a two stage particle separator for relativistic ions.

The first stage of the BigRIPS consists of 4 triplets of superconducting quadrupole magnets, combined with two dipole magnets at room temperature. Using a wedge-shaped degrader, a separation of primary and secondary beam can be performed. Heavy radiation shielding is needed because of this. The second stage of the BigRIPS is designed to identify and tag the different radioactive isotopes of the secondary beam cocktail. To achieve this, a host of different detectors is employed, namely position sensitive detectors for Bρ measurements, time of flight detectors for energy measurements, and ΔE detectors to identify nuclear charges. Thereby the momentum the atomic number and the charge to mass ratio of the beam particles can be determined on an event-by-event basis. After this apparatus a secondary beam of well identified isotopes can be delivered to the experimental stations.

The RIBF is currently one of the most advanced facilities for the production of radioactive isotopes. One constraint on the system is the maximum energy of the isotopes. The identification process by separation in the magnetic field strongly depends on the ionisation state of the ions. If velocities of the particles in the detector and degrader material are not sufficiently high, the ions can change their charge state around the equilibrium one. This leads to a significant reduction of the separation power but also misidentification especially in case of the most exotic rare isotopes.

The construction of the FAIR facility at the GSI, which would yield even higher energies than the RIBF would allow to circumvent this problem in the future.

Chapter 2

A detector setup for the (p,2p) reaction

2.1 Experimental concept

As described in section 1.3 a kinematically complete measurement of the two protons in a (p,2p) reaction is necessary to determine the Q-value (excitation energy transferred to the heavy residual) of the reaction. While a measurement of the proton energy is possible by using time of flight detectors, a precise measurement of the direction of the proton momenta demands highly segmented detector telescopes.

A measurement of the proton momenta, and thereby a measurement of the opening angles between the protons, and the angles between the protons and the beam axis, needs at least two measurement points on each proton trajectory. A system using single sided silicon detectors was designed (a detailed reasoning for this is given in chapter 3). It was decided to use two silicon strip detector planes for measurement of the x and z positions of one particle track (with z being the beam axis), and a combination of one silicon detector and a drift chamber, measuring the positions of the incoming beam particles, to determine the y values of one particle track. The three silicon detectors were positioned behind each other, forming one telescope arm. The whole tracker consists of two arms, meaning a total of 6 silicon detector planes. A schematic view of the tracker can be seen in Fig. 2.1. The angle between the two detector arms is 84°.

At low energies, the opening angle in a fully elastic scattering of two protons is 90°. Since the incoming nucleus possesses high kinetic energy, the Lorentz boost of the outgoing protons is non negligible, and leads to a maximum opening angle between the two protons of 84° at energies of 290 MeV/u. Therefore it is reasonable to assume a maximum of the proton distribution at angles of ±42° relative to the beam axis. This can also be seen in Fig. 2.4.

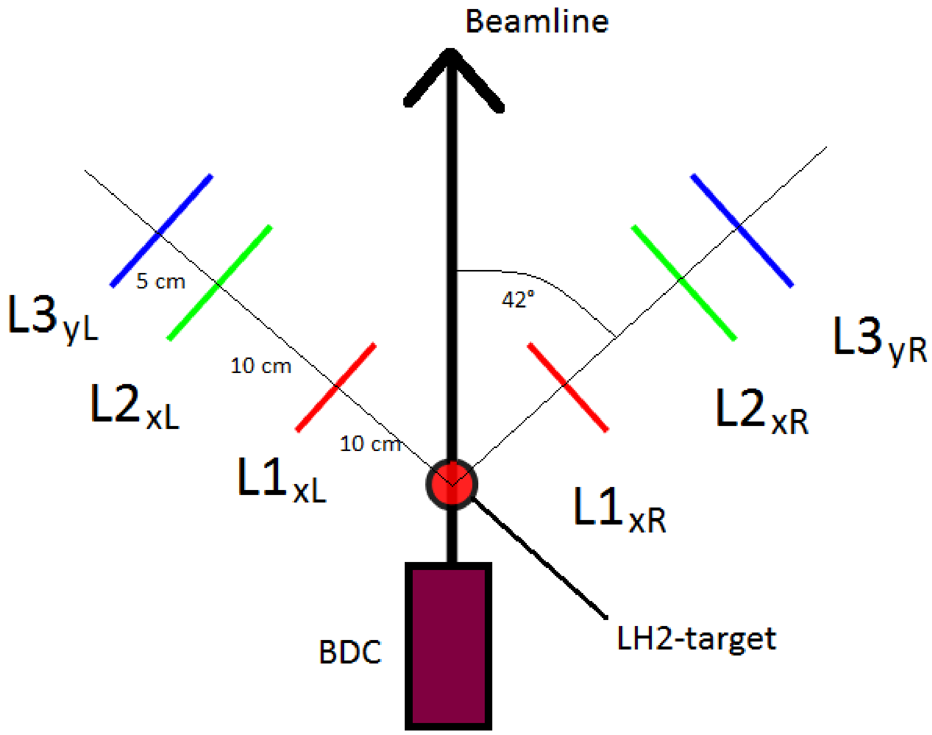

Figure 2.1: Schematic of a top view of the detector system. The black line marks the beam line (z-axis). The coloured lines symbolize the silicon detectors, the red circle marks the target position (size not to scale), and the purple box is a drift chamber for beam monitoring (BDC, not to scale). The red and green silicon detectors are used for determining x-positions, there strips positioned orthogonal to the plane of drawing, while the blue silicon detectors are used for y-position determination. The L1 detectors are 10 cm away from the target, the L2 detectors are 20 cm away, and the L3 detectors are 25 cm away. Details on the detectors can be found in section 3.1. The detectors have been drawn thicker than they are, for better visibility.

2.2 Simulation of detector response

A simulation of a simplified silicon tracker system for the measurement of fission barrier heights, using the (p,2p) reaction, has been performed using Geant4 and the event generator QFSC. QFSC simulates the proper kinematics of quasi free scattering events. It was developed by V. Panin. QFSC was used to simulate ^{16}O(p,2p)^{15}N reactions at a beam energy of 290 MeV/u. This reaction has been chosen due to the good experimental accessibility of the ^{16}O nucleus, and because the excitation levels of the ^{15}N isotope are well known, allowing for a comparison with existing data. The protons calculated by the QFSC where then implemented as particle sources into Geant4, while a two dimensional gaussian beam distribution, in the plane orthogonal to the direction of beam propagation, was taken into account. The beam was assumed to propagate into positive z-direction.

Three 150 μm thick, cylindrical polypropylene fibres where implemented as targets. They where placed vertically at z=0, with a spacing of 2 mm in x. Two silicon telescopes consisting of three parallel, 100 μm thick silicon detectors each where placed under angles of $\pm 42°$ relative to the z-axis in the xz-plane. The system was simulated to be inside a vacuum.

Since the detectors have been implemented as simple boxes inside a vacuum, the resolution of the detectors had to be implemented in a later stage. To simulated a silicon-strip-detector, each position value measured by the detectors has been assigned to a value on a grid with a spacing of 100 μm for the first and second layer, and of 200 μm for the third layer, as to simulate strip pitches of the same sizes. The detectors were assumed to be single-sided, with the first and second layer reading out the x-informations, and the third layer reading out the position information along the y-axis. For tracking, two x and two y values are needed for each track. Therefore it was assumed, that the y position at the target was known, as to simulate a position information of the incoming beam particle. This y position was then smeared out with a gaussian distribution, with σ=250 μm.

This values have been chosen due to the equipment used in the experiment described in chapter 4. The usage of a drift chamber to measure one of the y-values lead to a slightly lower resolution in y This has been done because of the angular straggling in the silicon detectors. Adding another silicon detector for y measurements would increase the total thickness of the telescopes. Simple calculations of the resulting angular straggling using the program ATIMA[1] yield values of 2.8 mrad for typical proton energies, which would mean a measurement error for a fourth

[1] https://web-docs.gsi.de/ weick/atima/

detector positioned 10 cm behind the third layer of over 270 μm. Therefore using a combined system of silicon trackers and a drift chamber was deemed to be superior.

Comparing the hits in two detectors behind each other, one can do tracking. Clear correlations can be seen in Fig. 2.2.

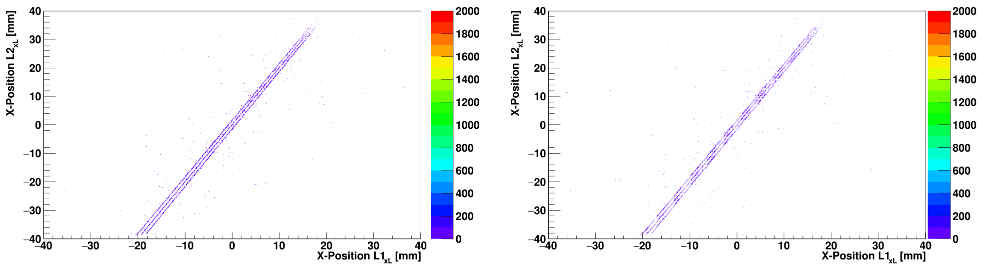

Figure 2.2: Tracking of the simulated (p,2p) reactions. The first two detectors in the left arm are shown, the second layer is plotted against the first layer. The image on the left is without detector resolution, on the right a resolution of 100 μm was assumed. The three target fibres are clearly visible. The influence of the detector resolution is minimal, since the resolution is dominated by angular straggling in the first detector layer, as can also be seen in Fig. 2.3

Using two position informations for one particle, a straight line can be interpolated, thereby reconstructing the particle track. If a track in the right and the left detector telescope can be reconstructed, the reaction vertex can be interpolated. This is simply done by searching for the point of closest approach between the two tracks, since an intersection between the two tracks is not necessary due to uncertainties from angular straggling and the detector resolution. The reconstructed vertex positions can be seen in Fig. 2.3, where the reconstructed x-positions of the reaction vertices are plotted.

To investigate the physical properties of the (p,2p) reaction it is necessary to investigate the opening angle between the two outgoing protons, this also being one of variables the missing mass depends on. The most straightforward way to do this, is to plot hits in a detector in the left telescope arm against the hits in the corresponding detector in the right arm, as shown in Fig. 2.4.

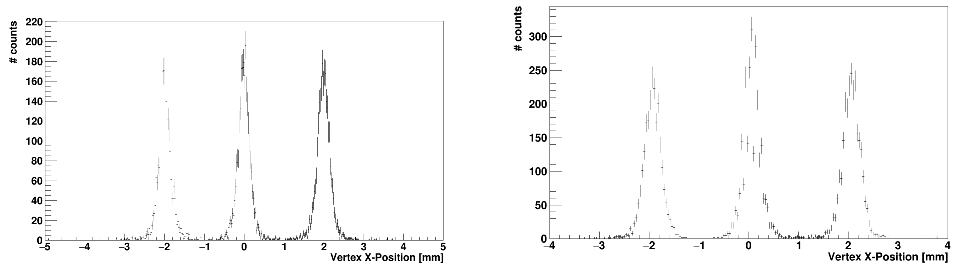

Figure 2.3: Reconstructed x-positions of the vertices. On the left side without considering silicon resolution, on the right with a silicon strip pitch of 100 μm. The influence of angular straggling in the first detector layer can be seen clearly, dominating over the influence from the intrinsic detector resolution. The average width of the peaks is 388 $\pm$ 3 μm in FWHM.

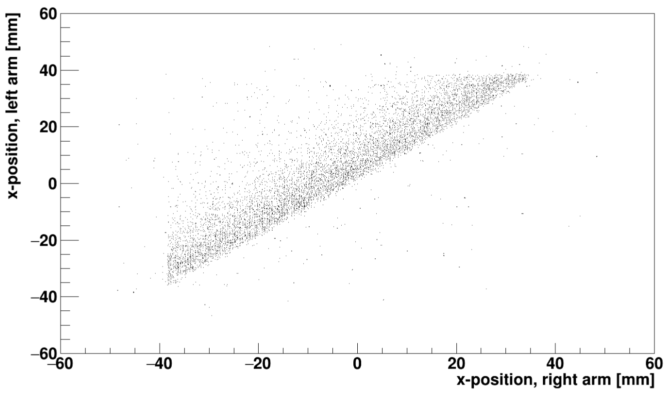

Figure 2.4: X-positions of the hits in the second layer detector of the first arm, plotted against the hit x-positions of the second layer detector of the right telescope. The maximum scattering angle of the (p,2p) reaction is clearly visible at 84°. Hits in regions with lower opening angles happen when the interaction between the incident proton and the nucleus is not a fully elastic proton-proton scattering, but also includes inelastic components between the incoming particle and the nucleus. Therefore lower angles correspond to a higher excitation energy of the nucleus. The sharp cutoffs at -40 mm and 40 mm are due to the geometrical constrains by the detector sizes.

For an analysis of the missing mass spectrum the energies of the protons also need to be known. Due to the low thickness of the silicon detectors simulated here, relating ΔE-ΔE information, gained from the silicon detectors to the energy of a proton would yield high uncertainties (compare Fig. 2.5). Because of this additional detectors are needed to extract the energy information of the protons.

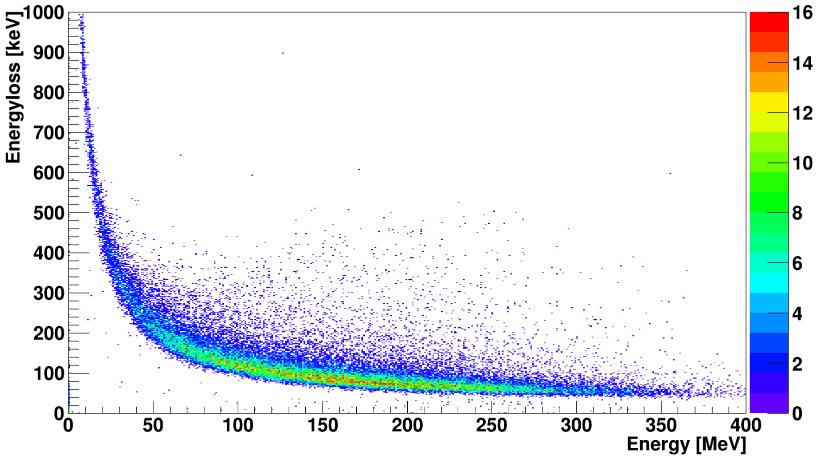

Figure 2.5: Proton energy deposited in one detector of the right telescope ($L1_{xR}$) on the vertical axis with respect to the total energy of the protons on the horizontal axis. For low energy protons a steep dependency is visible, but for higher energies this flattens out, making a distinction of different energies via the energy deposited in the silicon detectors impossible over a wide range.

Chapter 3

Detector development

Based on the knowledge gathered from the simulation described in chapter 2, a silicon tracker system was developed and optimized for the kinematics of the (p,2p) reaction. The system consists of a vacuum chamber with mounting and cooling structures for the detectors, and the detectors with the analogue read out electronics (in the vacuum chamber), and the digital read out electronics (outside the vacuum chamber).

3.1 Silicon detectors

As described in chapter 2, the thickness of the first detector plane determines the tracking resolution achievable with the described system. To minimise the overall silicon thickness in the system, it was decided to use single sided silicon strip detectors. The reason for this, is that single sided detectors of sufficient size could be provided by the company Hamamatsu with a thickness of 100 μm, while double sided silicon detectors would have had a thickness of 320 μm. This would have led to a Si-thickness in the first plane of 73.6 mg/cm^2, compared to 23 mg/cm^2 for a setup with single sided silicon detectors. The wafers used were capacitive coupled, with a resistance of 1.5 MΩ (nominal), and a coupling capacity of about 100 pF/cm per strip.

The first layer detectors have been built using one silicon wafer of a size of 7.84 cm x 5.1 cm. The active area of the wafer is 7.5523 cm x 4.93 cm. The strips are parallel to the shorter side (typeA, wafer layout in the appendix). For the second layer (which can be seen in Fig.3.2 on the left), two wafers of the same size have been used, with their strips aligned parallel to the longer side (typeB, wafer layout in the appendix). This gives a total active area of 9.86 cm x 7.5523 cm for the detectors of the second layer, with the bond pads for the readout at the longer side. Due to production, there is a small gap between the active area of the two separate silicon wafers, giving a small inactive area in the middle. The third layer detectors (which can be seen in Fig.3.2 on the right) each have been constructed out of two wafers

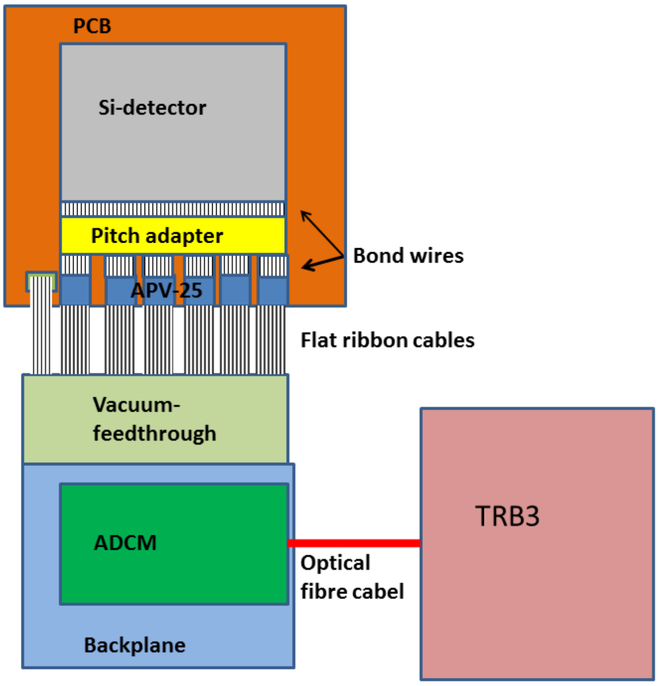

Figure 3.1: Schematic view of the detector setup for one detector, from the silicon wafer to the final part of the readout system. The silicon detectors are glued on a ceramic frame (not shown) which is itself glued to a pcb. Using bond-wires and a pitch adapter, the detector is connected to the APV-25 chips. Via a vacuum feedthrough the signal is then transported to the analogue to digital converter module which is connected to a TRB3 board via an optical fibre cable. The TRB3 board is connected to all silicon detectors and is used for event building and slow control of the system. For a detailed explanation of the parts, please refer to the text.

of typeA. Since this detectors were used to measure the y information, there strips have to be placed orthogonal to the first two detector layers. The strips of the two wafers have been connected with bond wires, giving one continuous strip over the full length of the detector, and a small passive area in the middle. Two of this strips were then connected and read out together, resulting in a spatial resolution of 200 μm, and thereby reducing the amount of electronics needed. Since the amount of angular straggling before the third detector layer will be more than σ_y>200 μm for protons at the expected energies, this should not result in a worsening of the achievable resolution. (A calculation using the program ATIMA [1] yields an average

[1]https://web-docs.gsi.de/ weick/atima/

angular straggling of 2.3 mrad for protons of E=150 MeV passing through a layer of d=46 mg/cm^2 of silicon.)

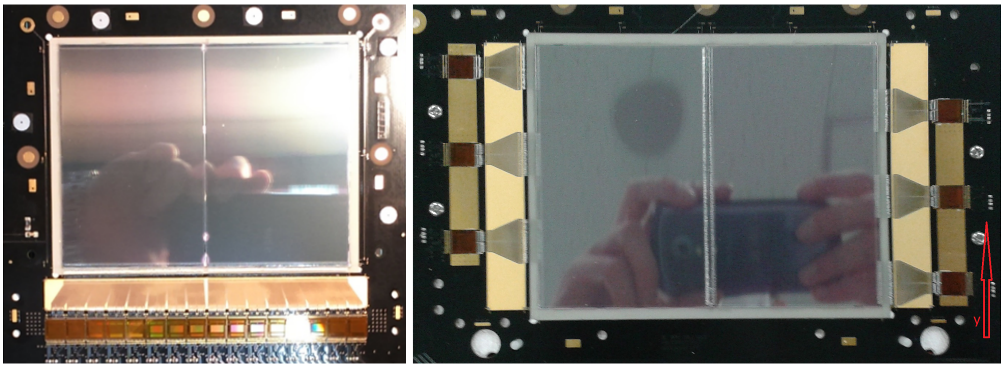

Figure 3.2: Detectors of the second (picture on the left) and third (picture on the right side) layer (not in the same scale). The detectors are placed as pictured, with the x axis in horizontal direction. The strips of the second layer detector run parallel to the y axis, the strips of the third layer parallel to the x axis.

The small thickness of the detector wafers makes them very fragile. To minimise thermal stress on the silicon wafers, they have been glued on aluminium-nitride ceramic frames with a thermal expansion coefficient similar to silicon. The stable ceramic frame was then glued to the pcb only on one edge, and on the two other corners, with a flexible silicon glue as to reduce the mechanical stress further.

A vacuum feedthrough has been designed, to connect the analogue with the digital read-out. It was chosen to use a simple pcb glued airtight into a aluminium frame. This was connected to the analogue read-out pcb via several 16-pin flat ribbon cables. An additional 16-pin flat cable is used for low voltage supply and communicating with the analogue readout ASICs (details in section 3.2) using the I2C standard. The connection to the digital part was done using a multipoint connector between the feedthrough and the so called Backplane. The Backplane is a pcb designed by Sebastian Reichert and used for voltage supply of the analogue read-out electronics, as well as signal transfer between the analogue and digital read-out, and for giving the detectors different numbers, thereby identifying the detectors, using a DIP-switch on the Backplane.

3.2 Analogue read out electronics

The electronics for the readout of the silicon wafers requires a high density while also providing a low readout noise and a minimum power consumption for components located inside the vacuum chamber. For analogue signal processing the APV-25 readout ASIC [22] fulfills this demands excellently. It provides full analogue signal processing, preamplifiing and shaping for 128 input signals, and a multiplexed output signal, while being limited to a maximum power consumption of 771 mW per ASIC. This allows for a very high input information density (128 channels at a chip width of 7100 μm), while reducing the amount of output channels to a minimum. The APV constantly writes its input signals into an internal 192 column analogue ring buffer, with at a frequency of 40 MHz. With its high readout frequency and the low power consumption the APV is ideally suited for the analogue signal processing for the silicon tracker. [22]

The interfaces to the APV were implemented in a specially designed detector pcb. Since the pitch size of the silicon detectors, at (d_S=100 μm) and the APV (d_A=44 μm) do not match, it was necessary to use a pitch adapter between the detector and the readout ASICs. A ceramic substrate material covered with tungsten, and a gold layer (l=100 nm) was used. The ceramic plates were processed, by using a laser for vaporizing the metal coating, thereby etching out the structure of the device [2]. Using 15 μm bond wires, the pitch adapters, APVs and silicon detectors were connected to each other.

Together with the digital read out electronics, this configuration allows for low noise levels as can be seen in Fig. 3.3.

Measurements of noise levels were done for each individual detector. For this, the detectors were mounted in a darkened chamber, and triggered randomly using the internal trigger of the TRB system (see Sec. 3.3 for a description of the TRB system). The electronic readout noise was measured by checking the APV channels not connected to the detectors. An average value of σ_{elec}=5 (ADC channels) was measured with only small fluctuations ($\pm$0.1 ADC channels) over all detectors. For detectors of the first and second layer, which were constructed bonding only one detector strip to each APV channel, the noise was below 10 ADC channels in sigma, at values fluctuating between $\sigma_{L1,L2}$=9.3 and $\sigma_{L1,L2}$=9.8)compare Fig. 3.3, 3.4. The third layer detectors had a noise level twice as high, at σ_{L3}=19$\pm$1 ADC channels. This can be understood as a result of the hardware combination of 4 single detector strips, increasing the input capacity by a factor of 4. Due to the short shaping time this input capacity dominates the overall noise figure.

[2]This was done by the company LaserMicronics

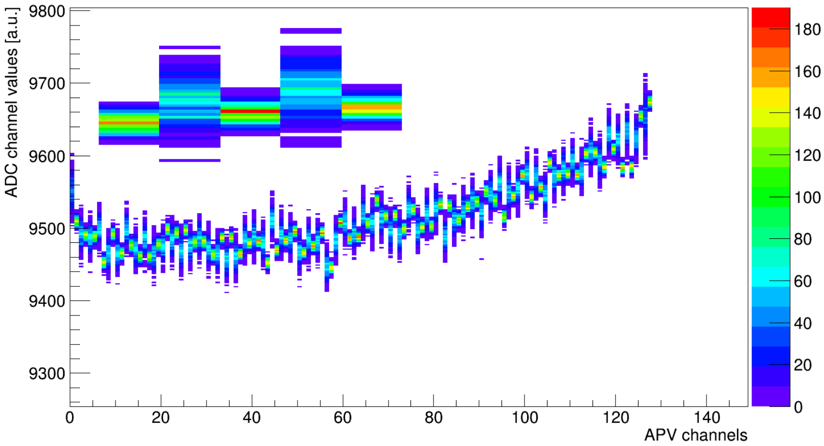

Figure 3.3: Base line measurement of one APV using a random pulse trigger. Plotted are the ADC channel values against the APV channel numbers. The channels 2-6 have been zoomed in on for better visibility. An odd even structure of the channels bonded to the silicon wafer and the channels not connected to the detector is clearly visible. A characteristic 'banana'-shape of the baseline is also well recognisable. For an explanation of both features please refer to the text. The noise values are σ_b=9.4 ADC channels in σ for the bonded, and σ_{nb}=4.8 ADC channels for the APV channels not connected to the detector.

Two features visible in Fig. 3.3 are the 'banana'-shape of the baseline and an odd-even structure of the channel noise. The APV uses a common voltage supply for all preamplifiers in one chip, supplied only to 4 points on the chip. This results in a voltage drop over the different channels of the chip, giving this characteristic "banana"-shape of the baseline. Correction for this is done in the digital read out electronics.

A well known problem of the APV-25 is the so-called common mode or baseline shift. When the APV-25 is getting a high input signal to a signle channel, the baseline of the APV experiences a localised pull down to lower values. The structure of this pull-down seems unpredictable. For further details see [23]. One solution to compensate this effect is to use reference channels without input signals. A comparison of the signal channels with the reference channels then allows to shift the baseline back, since a change in the reference channels output can only come from the common mode, or from electronics noise. This can lead to a slightly increased noise level, which is negligible due to the overall low noise level of the reference channels. It was decided to use every second channel of the APV as a reference channel not connected to the silicon wafer, giving the odd even structure and resulting in an optimal resolution for the deposited energy. (Considerations of error propagation lead to an approximate increase in common noise of less then 2 ADC-channels in sigma). With this scheme the correction can be performed in the ADCM of the digital readout (see section 3.3) to significantly reduce the amount of transferred data.

3.3 Digital read out electronics

For the digital part of data processing, electronic from the HADES-RICH detector [24] has been adapted for this detector system. The digital readout uses a TRB3 system as a central trigger unit. The trigger is then passed on to several state machines responsible for controlling the analogue to digital converters (ADC) and communication with, and trigger distribution to the APVs. Analogue signals from the APVs are then send back to the ADCs and the digital data is distributed to the TRB3 system which is responsible for event building and data traffic to the DAQ computers.

The connection between the analogue read-out part and the analogue to digital converters (ADCs) is done through the so called Backplane. The ADCs are part of a so called ADC module (ADCM), developed by Michael Böhmer [25]. This ADCM contains two 8-channel 12-bit ADCs, allowing for simultaneous digitalization of the input signals of 16 APVs. The digitalized signals are then fed into a FPGA on the ADCM. This FPGA allows for a whole series of digital signal processing features. First the base line correction as described in the previous section is performed. A channel mapping and zero suppression is performed as well as the interface to the TRB and also the correction of the baseline.

Based on special "pedestal runs" with randomly pulsed digital triggers corresponding baseline information is generated. Amplitude distributions for each channel are fitted with a gaussian distribution. The mean value of this fit is then subtracted from each event measured in this channel, allowing for a flat baseline (compare Fig. 3.4). The σ-values of this gaussians can also be used for calculating values for zero suppression. To reduce possible influence from fluctuations in the voltage supply and distribution, this has to be done once after every switching on the system.

An option for zero-suppression, where the FPGA uses externally computed cut-off values, is also implemented into the ADCM, allowing for a massive reduction in used output bandwidth and storage capacity. Together with storage units the FPGA allows for packaging several events together (distinguishing them through their

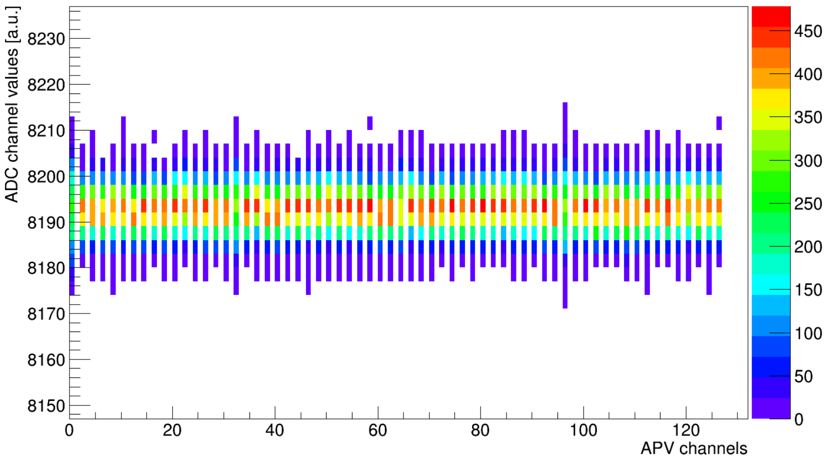

Figure 3.4: Signal amplitudes of one APV after applying baseline correction and common mode correction procedures. A correction for the baseline has been applied, and unbonded channels have been removed by the FPGA on the ADCM to decrease data transfer on the network. The baseline is flat, with almost no fluctuation. The constant noise level is achieved.

trigger number), and sending them via an optical fibre cable to the TRB3, using the UDP standard for communicating. The possible buffering of events in the ADCM allows for a reduction in network traffic and can thereby increase the possible trigger rates.

The TRB3 board is a circuit board developed by the HADES collaboration [26] for trigger handling, event building, and communication between detector systems and users through a network switch. For this purpose, the board uses the DHCP communication standard. The TRB3 uses a central FPGA for this purposes, and 4 secondary FPGAs for communicating with the subsystems, which are connected via specialised interfaces. Just as the ADCM, the TRB3 also uses an internal memory to buffer events, and thereby make an optimal usage of network resources possible. [27]

The TRB3 system uses 32-bit words for data transfer. Data from the ADCMs is structured in a straightforward way. The first bit is an error bit, signalling if the event should be used. It is followed by a 6-bit identification number, set by DIP-switches on the Backplane. Then 4 bits containing the APV-number follow (this number is set through bonding on 4 APV pads [22]). 7 bits with the APV channel number follow.

After this, the ADC output information follows in the last 14 bits (since the ADC used only has a 12 bit resolution, the first two bits are not used). [28]

During most actual data takings, a zero suppression will be performed to reduce data traffic on the network. If the detector system is triggered by the external trigger, the full (p,2p)-tracker system would produce 8704 32-bit words per event. Ignoring all unbonded channels, after they have been used to correct for baseline shift, reduces this to 4352 data words. Ignoring channels from parts of the APVs not connected to the detectors would reduce this further to 4273 words, or 17 kByte per event. Of this 4273 words typically less than 6 contain the information of the (p,2p)-reaction. Using zero suppression, for example with an electronics threshold of $T_{elec} = 3\sigma$, this 4273 words can be reduced to an average of 12 words in addition to the hit information. If a typical event has for example a multiplicity of 3 in each detector, this would mean a total of 30 words would be sent from the ADCMs into the network, reducing the event size from 17 kByte to 120 Byte. Only if data cannot be transferred to the data aquisition (DAQ) PC for to long the memories built into the TRB system fill up making dead time necessary, to send the data to the DAQ-computer. Typical experimental data for one APV using zero suppression can be seen in Fig. 3.5.

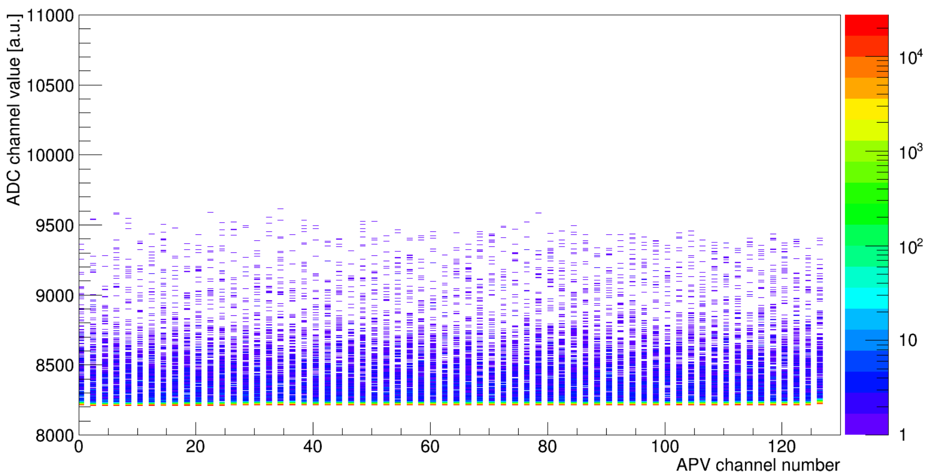

Figure 3.5: Signal distribution in one APV-25. The picture was taken during beam time, with the same corrections as in Fig. 3.4. Additional zero suppression was performed, as described in the text above. The cut-off at about 9500 is due to the APV dynamic range. An artificial offset of 13 bits is added to avoid negative numbers.

3.4 Dead time free system integration

The silicon tracker system described here is designed to be a modular detector system compatible with any number of different setups. For this purpose two input signals have to be given to the silicon tracker. First an external trigger signal is needed, since the system is not self triggering, and second a time stamp is needed to ensure synchronization with the other detector systems used. The silicon tracker described here can be integrated in any system providing these two signals, without adding dead time to the system, provided that the network bandwidth for the DAQ is high enough.

Since the APV-25 is not self triggering, an external trigger timing has to be supplied during experiments. This external trigger is fed into the TRB3 for trigger handling. The TRB system then allows to monitor trigger rates and resulting network traffic. A simple additional circuit board allows for a trigger distribution to all included ADCMs, using CAT5 cables. For testing purposes it is also possible to trigger periodically, or randomly distributed around a certain frequency. During tests of the full silicon detector system using the internal trigger of the TRB3, trigger rates of 80 kHz were possible for the full system, without introducing dead time.

This is possible due to the nature of the APV and the digital electronics used. An APV chip will always readout the input channels and save them to an internal ring buffer at a high frequency, ensuring that every signal could be read. This advantage of the APV is further enhanced by the used digital readout electronics. When a trigger is send to the APV, the ASIC will send the corresponding memory entry in its ring buffer as output. High speed ADCs on the ADCM ensure for a quick conversion of this signals into digital data, which is then stored on the ADCM. When network traffic with the TRB3 board is possible, the ADCM will send packages containing this data to the central board. In most situations it is preferred to switch to a mode that will allow the buffering of several events, packing them together, to optimally utilize the UDP communications format.

The TRB3 board itself will do the event building, and safe the events in internal buffers, until full DHCP package size is reached, or in a different configuration, each event will be send separately, depending on the method best used for other parts of the whole experiment. With this method of buffering and high speed electronics, the detector system described here allows for high readout without dead times, as long as the memory buffers do not overflow.

For synchronization with other detector systems, the silicon tracker described here allows for time stamping. This is done via an addon board on the TRB3, which allows to send external signals via a lemo cable to one of the FPGAs of the TRB3. Firmware programmed by Ludwig Maier [29] allows to use this input signal as a time stamp. For this, the input signal has to send a clock at a frequency of 40 MHz over the cable. The FPGA will then count clock cycles, and, when a trigger is provided will send the number of clock cycles to the central FPGA of the board, where it is added to the event data, effectively giving a time stamp to every event. This allows for controlling synchronization between the silicon tracker system and other detector system. With this method, event mixing can be ruled out for any larger detector system.

In praxis, this modular approach has been used at the experiment performed at the HIMAC facility (see chapter 4 for details on the experiment). Several different detectors have been used together with the silicon tracker system. The trigger has been provided externally by the scintillator hodoscopes used (see section 4.2 for the trigger logic), and all events have been time stamped. The performance of the silicon tracker during this experiment was excellent, with all parts running at their full capacity.

Chapter 4

Experiment at HIMAC

Before using the full detector setup together with the SAMURAI spectrometer in a radioactive beam experiment at the RIBF a detailed experimental performance test had to be performed. This test was performed at the Heavy Ion Medical Accelerator in Chiba (HIMAC) in Japan, using a ^{16}O beam with an energy of 290 MeV/u.

4.1 The HIMAC facility

The HIMAC is a heavy ion cancer treatment facility in Japan. It can provide stable ion beams from protons up to xenon, which are used in medical treatment as well as in research. In cancer treatment heavy ions provide several advantages compared to normal radiation therapy. Accelerated ions like carbon have a far higher effect on irradiated tissue, making them more effective in destroying cancer cells. [30] Additionally, the sharp Bragg peak of the energy deposition of heavy ions as a function of tissue depth allows for a very precise targeting of cancer cells in certain positions, by modifying the beam energy, and thereby the position of the Bragg peak. [31]

Besides cancer treatment, the HIMAC facility is also used for research in the fields of biology, chemistry and physics. It uses 3 ion sources to provide stable beams of ions from protons to xenon. [32] A linear accelerator serves as injector into one of two synchrotrons which yield energies up to 800 MeV/u. This ion beams are then transported to research stations or to the treatment stations. [33]

Since during the day HIMAC is used to treat patients, physics experiments take place in the night. In total 5 nights of beam time were approved for the experiment discussed here. 4 nights were dedicated to ^{16}O beam at an energy of E=290 MeV per nucleon. In the last night a ^{132}Xe beam at 290 MeV/u was used. The rate of incoming ions was chosen to be between $R=2 \cdot 10^5$ pps and $R=4 \cdot 10^5$ pps for the oxygen beam and between $R=1.3 \cdot 10^4$ pps and $R=1.2 \cdot 10^5$ pps for the xenon beam. The beam spot size at the entrance window of the detector chamber was monitored

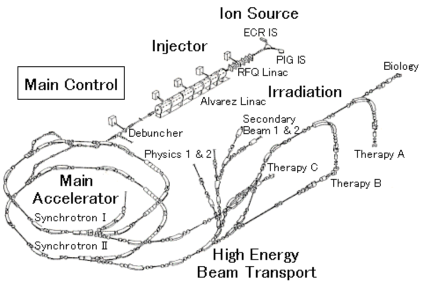

Figure 4.1: View of the HIMAC accelerator facility. Ion sources, the injector, the synchrotrons and the experimental and therapy stations are shown. Taken from [33]

on a daily basis using a scintillation screen. Typical dimensions of $\Delta y \sim 10$ mm in vertical direction and $\Delta x \sim 5$ mm in horizontal direction were used in the different periods of the measurement with a rather stable integrated rate. A total of 17021553 events were triggered (for details on the trigger conditions, see section 4.2). A rate estimation has been performed. Cross sections have been taken from [34] and [35]. A rate of 10^5 beam particles per second has been assumed. Angular coverage of the detectors has been taken into account. All together this yields, for the (p,2p) reaction with a 7 mg/cm^2 CH_2 target, a rate of 0.05 Hz.

4.2 Detector setup

The setup used in the experiment can be seen in Fig. 4.2.

For beam monitoring a ArC_2H_6 (50/50)-drift chamber (BDC) with a gas volume of approximately 20 litres was used. The drift length of the BDC is 9 mm and the half gap of the chamber is 6 mm, with an effective area of 126x126 mm. Using a structure of 10 wire planes, alternating between x and y position measurements, the drift chamber allows for a determination of position and momentum direction for the incoming beam particles. The wires were supplied with a voltage of 2 kV for the oxygen beam and with 1.3 kV for the xenon beam. For the drift chamber a position resolution of $\sigma_{x,y}$=800 μm could be achieved.

Two scintillator layers have been placed as the first detectors hit by the beam. This was done to give a timing information for a beam particle entering the system. For triggering the detector system, the hodoscopes were used. For one of the plastic scintillators to be triggered, signals from both photo multipliers of the scintillator were demanded. During most of the beam time only events which triggered a scintillator in the left as well as in the right hodoscope were recorded. This allowed

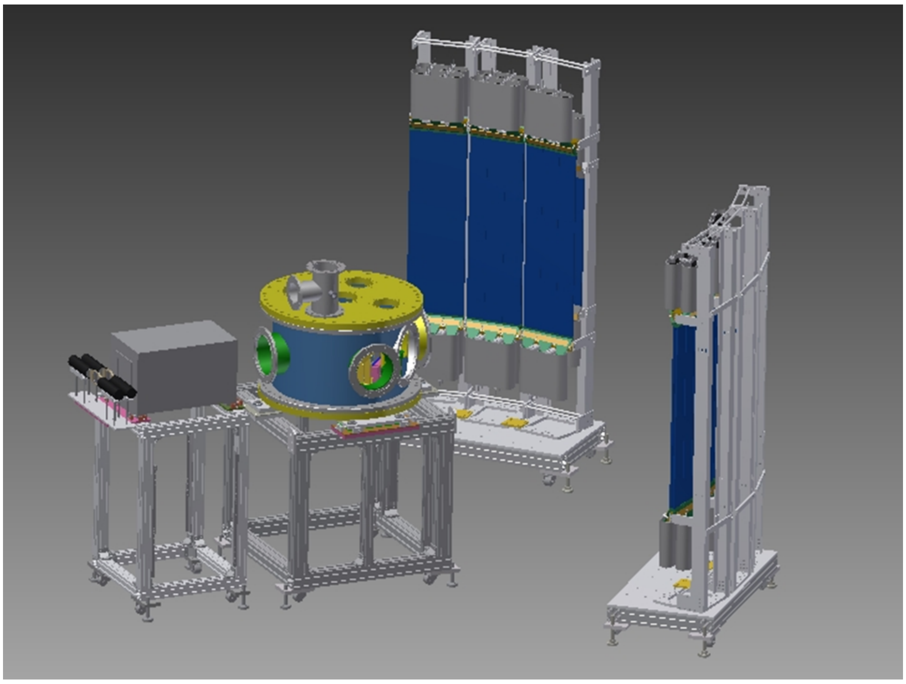

Figure 4.2: Schematic of the detector setup at the HIMAC facility. The grey box on the left is a drift chamber, with two plastic scintillators left of it, used for determination of the start time. The cylindrical target chamber contains the full silicon detector setup discussed here as well as the target station at its center. Windows for the beam and protons can be seen on the side of the chamber, as well as the opening for the vacuum pump on the top. Two large area plastic hodoscopes complete the setup. For more details please refer to the text.

for a reduction in the trigger rate, limiting the amount of data traffic and reducing the number of "good" events lost due to dead time in the systems.

The hodoscopes consist of plastic scintillators on polyvinyltoluene basis [1] of a width of 10 cm a height of 100 cm and a thickness of 1 cm. On the top and the bottom of this scintillator photo multipliers have been glued onto them with optical glue. Together with the plastic scintillators in front of the drift chamber, this allows an analysis of the time of flight, which allows for a energy reconstruction for protons emitted from the target. The two hodoscopes are placed centred on the same spatial axis as the silicon telescope arms, with a distance of d=160 cm to the target position. Each hodoscope consists of 9 plastic scintillators, which are placed touching each other. They are placed with a curvature, as to give each scintillator the same distance to the target, simplifying the ToF analysis.

[1]more specifically the EJ-200 material from the company APACE Science

A special detector configuration for particle identification was placed on the beam axis about 3 m downstream of the target position (not shown in Fig. 4.2). It is a combination of plastic scintillators, CsI detectors and an iron degrader. A 22 mm thick iron degrader is followed up by four consecutive plastic scintillators with a thickness of 3 cm each. This was designed to stop nitrogen atoms in the first scintillator, while lighter ions should pass through to following detectors, allowing for a separation based on the nuclear charge. At the end of the detector system CsI detectors have been placed, to stop lighter ions and allow for a ΔE-E based particle identification for most lighter ions.

4.2.1 Vacuum chamber and silicon tracker

The vacuum chamber used in this experiment is a 60 cm diameter aluminium chamber with a total of six windows. Two are used for beam entry and exit, two windows are used as exit windows for the protons, and two are windows closed with transparent plastic, allowing for an optical control of the chamber inside without breaking the vacuum. The four windows are made from 125 μm thick Kapton[2] foil. The target is placed in the center of the chamber, with the plane of the holding structure perpendicular to the beam axis. The six cooling frames as well as the structure for mounting the target have been fixed by screws and positioned precisely through the use of alignment pins, giving a position accuracy of 0.1 mm. To ensure precision of all positions relative to each other, all alignment structures have been milled into the bottom flange of the vacuum chamber with a manufacturing tolerance of 0.1 mm.

The floor of the target chamber was positioned parallel to the xz-plane of the whole setup, with the beam direction defining the z-axis, and the y-axis being the upward direction. The silicon detectors were placed as described in chapter 2 under angles of $\pm 42°$ relative to the beam axis, at distances of 10, 20 and 25 cm from the target. The plane of the detectors was positioned perpendicular to the line between the center of the target and the center of each detector. To ensure the precision of the placement of all parts, the positions of the target and the detectors relative to the vacuum chamber was determined using a photogrametric system, which uses reflective points sticking to the structures. A picture of the open vacuum chamber, were the target has been replaced with an additional silicon detector for tests of the readout system using cosmic rays can be seen in Fig. 4.3.

---

[2] Kapton is a trademark polyimide foil of the DuPont company

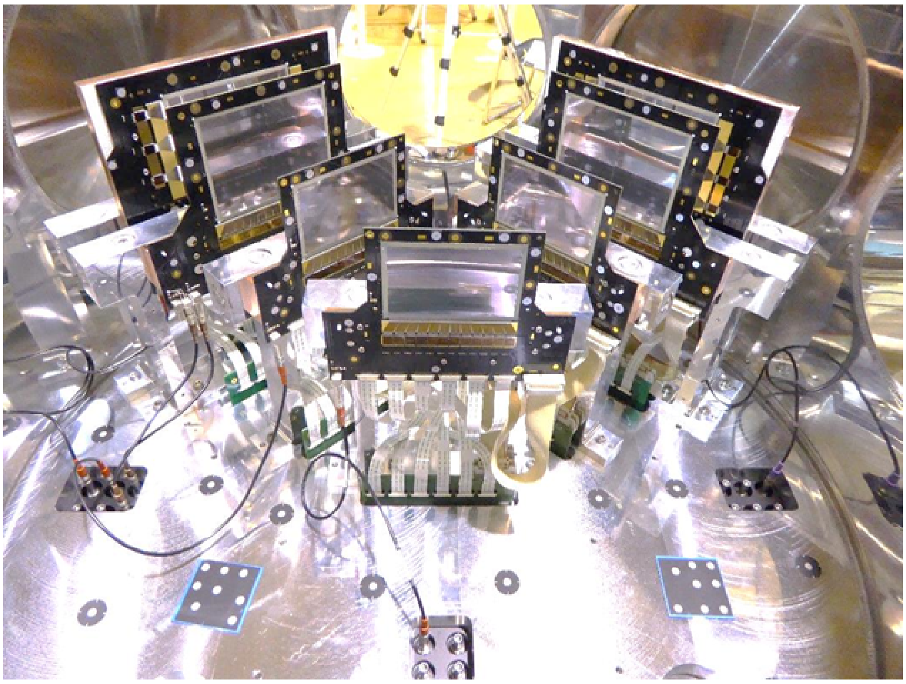

Figure 4.3: Photo of the open vacuum chamber. The two detector arms are visible, as well as a seventh silicon detector at the center of the chamber, used for cosmic ray measurements. In the experiment it is replaced by the target. The beam direction is from the bottom to the top of the picture.

4.2.2 Target

Several requirements had to be fulfilled by the targets designed for the experiment. Targets have to be positioned precisely (with an uncertainty of 0.1 mm). Besides this, the thickness of the targets has to be known as precisely as possible, to allow for an accurate determination of reaction rates. The material of at least one type of target has to contain significant amounts of hydrogen, acting as protons for a (p,2p) reaction. Since pure hydrogen targets are difficult to handle, several polymers are possible alternatives. The high amount of carbon contained within them makes the use of calibration targets made from carbon necessary.

It was decided to use a design of several clearly separated layers. For this a holding structure was built that allows for a precise positioning of the targets as well as for changing the targets without opening the top lid of the vacuum chamber. Replacing the targets was done through the side windows. The targets consist of an aluminium frame (65 mm x 70 mm) with a rectangular opening in the middle

(45 mm x 40 mm). The frames are fixed on the basic mounting structure. This allows for flexible positioning of different target frames. The target materials are glued on the frames. Together with aluminium distance holders this allows for positioning several well separated target layers. The holding structure, together with several frames can be seen in Fig. 4.4.

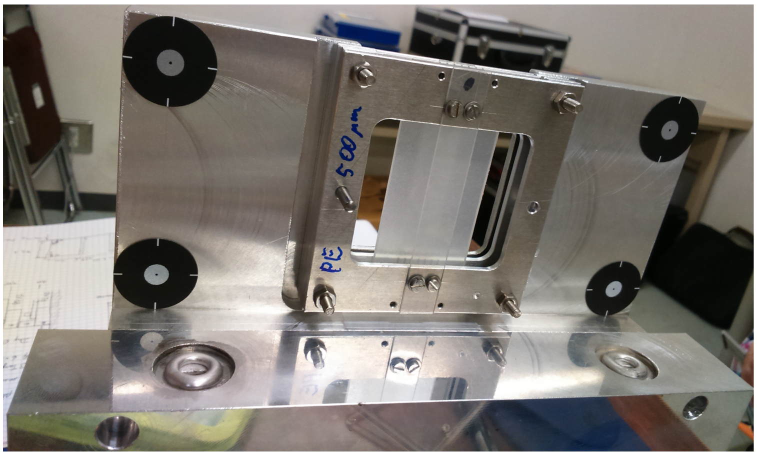

Figure 4.4: The holding structure for the targets can be seen. Several aluminium frames with PE-targets are visible, mounted on the base structure. On the four corners optical markers used for position determination have been glued on.

Four different target materials have been chosen. Polypropylene, polyethylene, graphite and diamond. A diamond target has been built with a thickness of 56 μm. The graphite target had a thickness of 110 μm. Both carbon targets covered the whole beam spot and were glued on a mylar foil with a recess, eliminating background from the foil, which was then connected to the aluminium frames. Polypropylene targets have been built from cylindrical fibres with a thickness of 150 μm. This fibres have been positioned with high precision (σ_{fibre}<0.1 mm) on both sides of the 2 mm thick frame. The fibres were positioned with a spacing of 2 mm in machined slits to guarantee for a distance of 200$\pm$0.05 mm between the centres of the two layers of wires. The fibres one the back side were shifted horizontally by 1 mm compared to the fibres on the front side. One polyethylene target has been built with a thickness of 1.2 mm, covering the whole plane. Two were constructed from 1 cm wide and 0.6 mm thick polyethylene strips. The thinnest polyethylene targets were built from 100 μm thick foil. In this foil a hole structure has been drilled. It consisted of holes of 0.7 mm diameter and of holes with a diameter of 0.3 mm. An alternating pattern of this holes was drilled, as to allow identification of the position on the foil. The hole pattern of this foil could not be resolved in the experiment, as the estimation for the drift chamber resolution used for determining the y-positions of the beam particles turned out to be to optimistic.

Chapter 5

Data analysis

The analysis of the data makes it necessary to first identify particles and separate them from noise. After this tracking of the particles in the silicon detectors takes place. If two full tracks are identified in one event, the reaction vertex position can be interpolated from them. After this, an additional cut on the outgoing nuclei allows for an identification of (p,2p) reactions.

5.1 Particle identification and tracking

The first step performed in the data analysis was to look at the separation of particle signals from the electronics noise. This has partly been done in hardware, as described in chapter 3 but a more detailed view is essential here to evaluate the detector performance. Plotting the recorded signals above threshold in the first detector of the left arm against the signal amplitudes of the second detector of the left arm, as shown in Fig. 5.1, shows a clear distinction of particle signals.

The next step after identifying particles is to plot hit positions of the first against the second layer for each telescope arm. This allows for tracking particles in the detector arms. See Fig. 5.2

From the spatial correlations shown in Fig. 5.2 emission points of particles along the beam line can be deduced directly. This is done by intersecting the beam line with the extrapolation of the two dimensional tracks. This yields values in three distinct regions. The interpolated values for the two tracks in the upper left corner can be seen in Fig. 5.3. The main track originates around the zero value, coming from the target. The less pronounced track in the upper left corner can be interpolated to come from a position roughly 40 cm up stream of the target. At this position the Kapton entry window of the target chamber is located (precisely 45 cm upstream of the target, the values match within the uncertainties). The third track is estimated to come from a position at around 110 cm (with a high uncertainty) up stream. At this position the plastic scintillators triggering the system are located.

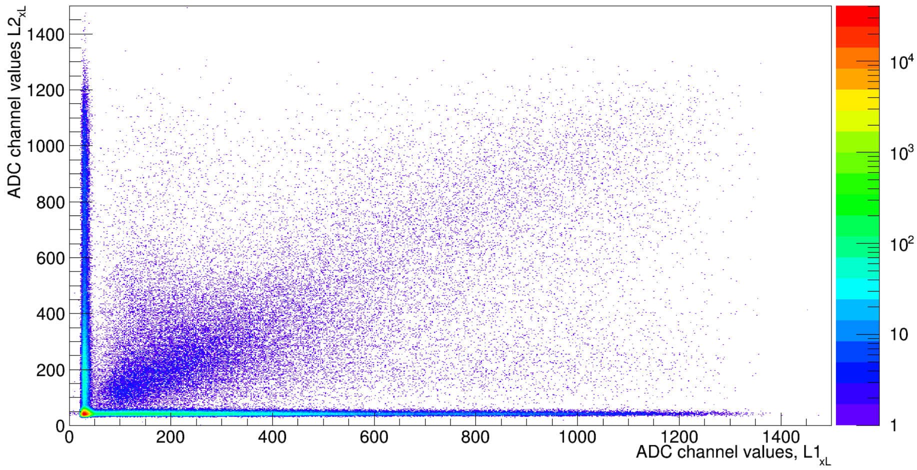

Figure 5.1: Signal amplitudes in the second detector of the left arm ($L2_{xL}$) against the first detector of the left arm ($L1_{xL}$). The ADC channel values have already been corrected for baseline offset. The noise and the cutoff values can be seen well. The distinction between noise and particles is clearly visible, since at a 3σ noise suppression still 0.5 % of the channel amplitudes will excel the hardware threshold at around 25 channels.

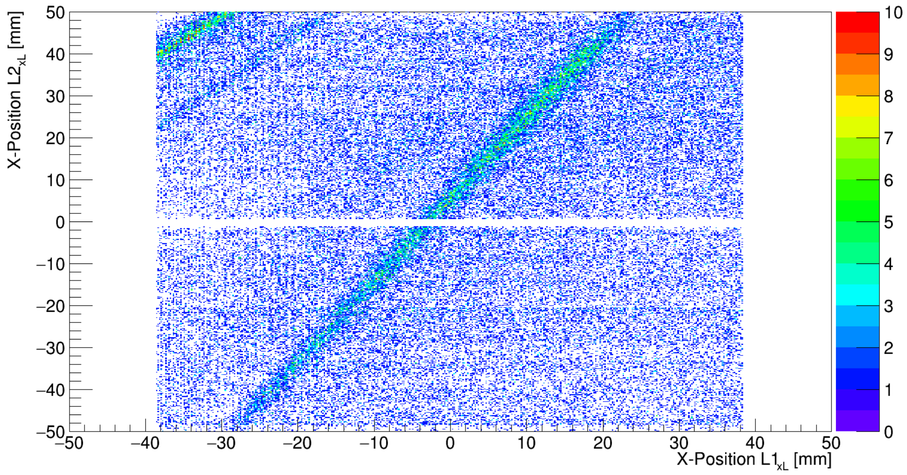

Figure 5.2: The plot shows x positions of the hits in the second detector layer (detector $L2_{xL}$) against the first layer (detector $L1_{xL}$) for the left telescope arm. The most pronounced feature is the central diagonal indicating particles from the target point. In the upper left corner two additional tracks indicating additional sources of particles can be seen (see text for details). Additionally a gap can be seen around the zero value of the x position in detector $L2_{xL}$. This is due to the physical gap between the two silicon wafer in the second layer.

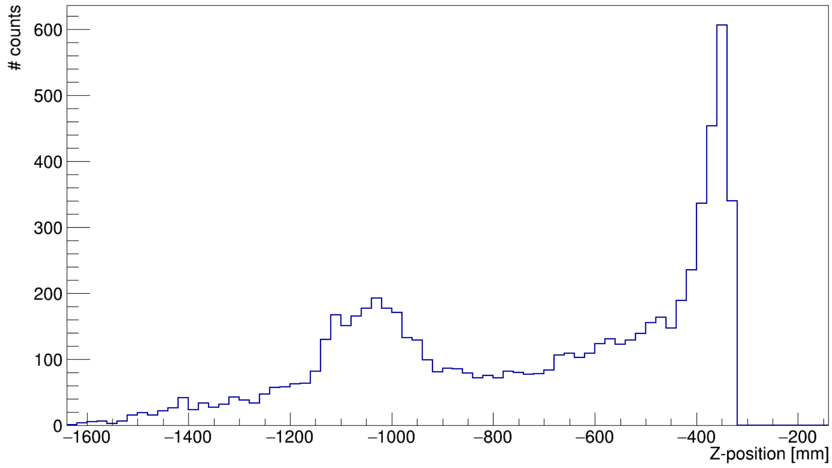

Figure 5.3: The calculated intersection between the second and third most pronounced tracks and the beamline are shown. Two distinct peaks are visible, one at roughly 30 cm and a very broad peak at 110 cm. The high background between the two peaks is most likely to come from reactions in the drift chamber.

Similar considerations can be made for the right side of the detector system. The corresponding picture can be seen in Fig. 5.4. Extrapolating tracks back to the z-axis yields the same values as for the left side, verifying the argument from above.

Gateing on tracks originating from the target position can be done, by cutting out all events outside the central correlation on the left and right side seen in Fig. 5.2, 5.4. This allows for analysing only events with exactly two detected tracks, coming from the target. Using the two particle tracks, it is now possible to try to reconstruct the vertex positions. This can be done by interpolating the particle tracks and searching for the points of closest approach, which should yield the vertex positions. While the x positions can be extracted from the silicon tracker system alone, for y positions it is necessary to use information from the drift chamber combined with the third detector layer to reconstruct the full track.

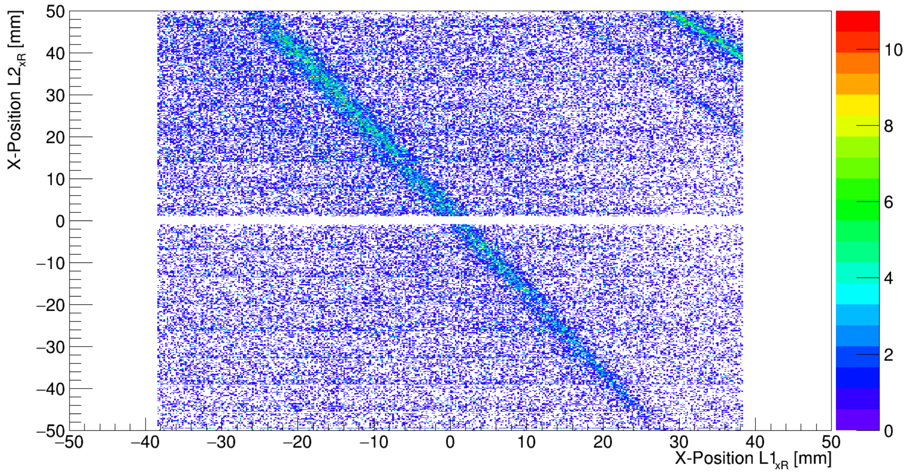

Figure 5.4: The plot shows x positions of the hits in the second detector layer (detector $L2_{xR}$) against the first layer (detector $L1_{xR}$) for the left telescope arm. The most pronounced feature is the central diagonal indicating particles from the target point. In the upper left corner two additional tracks indicating additional sources of particles can be seen (see text for details). Additionally a gap can be seen around the zero value of the x position in detector $L2_{xR}$. This is due to the physical gap between the two silicon wafer in the second layer.

5.2 Vertex reconstruction

To make a precise reconstruction of the vertex possible, it is necessary to know the detector positions with similar precision. Therefore a photogrammetric system has been used. For this, the detectors have been marked with several reflective points. Additionally the vacuum chamber is also marked as a reference. A specialised recording system then allows to get the relative positions of all the points, which, together with the known position differences between the points, makes it possible to reconstruct the positions of the detectors relative to the reference points, with an accuracy up to 100 μm.

Altogether this yields precise measurements of the hit positions, in the coordinate system of the vacuum chamber. With this the reconstruction of the vertex positions (using the algorithm described in chapter 2) is possible in a very precise manner. To check the quality of the reconstruction, data from a beam night with a target of polypropylene fibres was analysed. Results for the x and z vertex positions can be seen in Fig. 5.5.

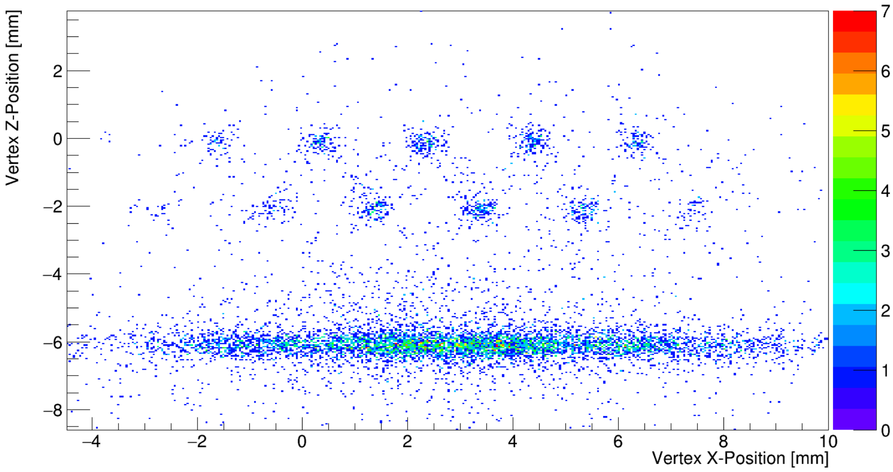

Figure 5.5: X-positions of the vertex reconstruction, against the z-positions. Clearly visible are particle tracks originating from the foil target at the z-position of -6 mm. The two planes of polypropylene fibres at -2 mm and at 0 are well separated. The distinction between the fibres in the x-direction is also clearly visible. The events between the two fibre planes at z=0 mm and z=-2 mm show a clear pattern of events where one of the outgoing protons hit the second fibre layer and was scattered there.

For a more quantitative analysis of the resolution the results shown in Fig. 5.5 are projected onto the z-axis, as can be seen in Fig. 5.6. The three distinct peaks allow for a comparison of rates in the different target planes. The rate difference visible is mainly due to the different target sizes in the xy-plane. This can be estimated by comparing the effective mass of the polyethylene foil with the size of one fibre target plane. One fibre target plane covers 150 μm per 2 mm in x, while the foil covers the whole x-area illuminated by the beam (this amounts to densities of ρ_{foil}=9.15 mg/cm^2 and ρ_{fibre}=1.035 mg/cm^2). This suggests, that the ratio of the peak heights (foil/1 fibre plane) should be 0.075. The ratio of counts in the peaks is 546/6767, or 0.081, being in good agreement with the estimated. Differences are due to the different materials and the cylindrical form of the target fibre. The position resolution in z can also be extracted from this plot, by looking at one peak. This gives a value of 553 μm in FWHM for the peak of the foil. The estimation detailed in section 4.1 suggests a total of 4860 counts for the foil, compared to the measured 6767 counts. Both numbers are in the same order of magnitude, validating the estimation.

It is now possible to gate on a single plane of the target. This allows to analyse the vertex x-positions for each plane. This yields the pictures in Fig. 5.7. In total

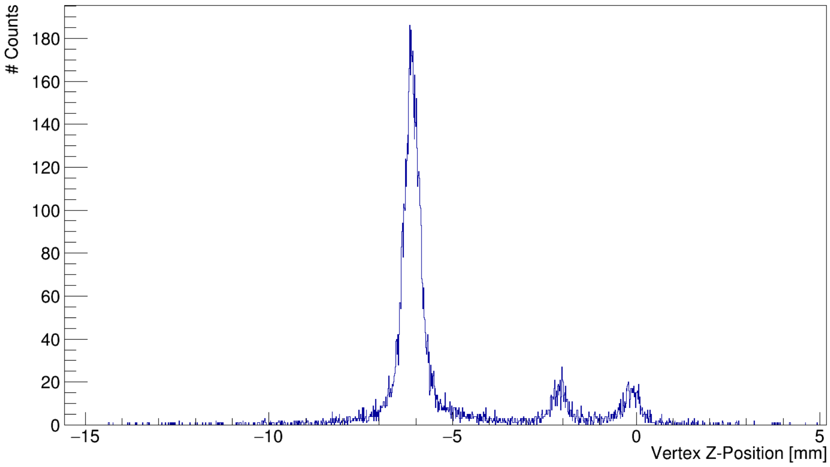

Figure 5.6: Intensity against z-positions of the vertices. The three different peaks come from the three planes of target material. For a discussion of the peak heights please refer to the text.

11 peaks are visible, 8 of them with sufficient statistics to perform a reliable fit. On each of this peaks a gaussian has been fitted, and the average has been calculated. (values are listed in table 5.1). The resulting resolution is Δ_x=412 $\pm\,^{12}_{28}$ μm in FWHM. This compares to $\Delta_{x,sim}$=388 μm given by the simulation, meaning that the system is very close to its theoretical limit. The deviation most likely comes from small uncertainties in the detector positioning.

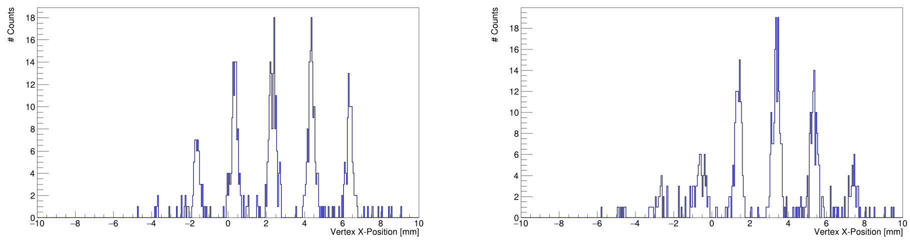

Figure 5.7: Intensities against x-positions of the vertices. The left picture shows the fibres of the plane at z=0. On the right side the fibres of the plane at z=-2 mm are shown. The peaks are well separated, with nearly no background. The intensity distribution of the incoming beam can clearly be seen. The resolution averages to 412 μm in FWHM.

x [mm]	z [mm]	FWHM [μm]	Δ_{stat} [μm]
-1.6	0	353	40
0.35	0	360	21
2.4	0	466	21
4.4	0	367	19
6.3	0	356	26
1.4	-2	407	49
3.4	-2	457	19
5.3	-2	535	31

Table 5.1: Resolution values for the fibre targets. X and z positions of the peaks are listed together with the extracted FWHM value. Values have been calculated from Fig. 5.7. The x positions of the peaks are expected to be at positions 0.5, 1.5 .... The position uncertainty due to the production process of the fibre target is at 0.1 mm. The mean value of the peaks are correct within the uncertainties.

5.3 (p,2p) reaction

The next step in the analysis is to identify (p,2p) reactions. A first selection of events could be performed by selection of the heavy reaction product in the ΔE-E detector. Here all ^{16}O(,)^{x}N reactions could be identified. With this it is possible to identify nitrogen atoms coming out of the chamber. This gate allows to identify any reactions knocking out one proton out of the incoming oxygen ions. It is still possible for reactions who knock out a proton and several neutrons of the ^{16}O to pass through the gate. Reactions with two outgoing particles of different mass are unlikely to hit both silicon telescopes, because of the asymmetric kinematic of this reactions. Reactions producing two, or more heavy particles would imply a fragmentation of the nucleus, meaning that a highly inelastic process would have taken place. This would result in low transversal momenta of the products compared to the momentum of the nucleus before the interaction, making it highly unlikely for two particles to hit the detector system in both arms simultaneously. To check for the validity of the gate, the correlations between the left and right detector arms can be checked (Fig. 5.8). The correlation is clearly visible. It shows all the properties expected from a (p,2p) reaction, meaning that the gate is well placed.

It is possible to extract an opening angle between the two protons from the information in Fig. 5.8, when combining it with y-information from the detectors and the drift chamber. This results in Fig. 5.9. The sharp edge at 84° is well pronounced. The typical structure with the smearing out to smaller opening angles can be seen. For a full analysis of the Q-value the energy of the protons has to be

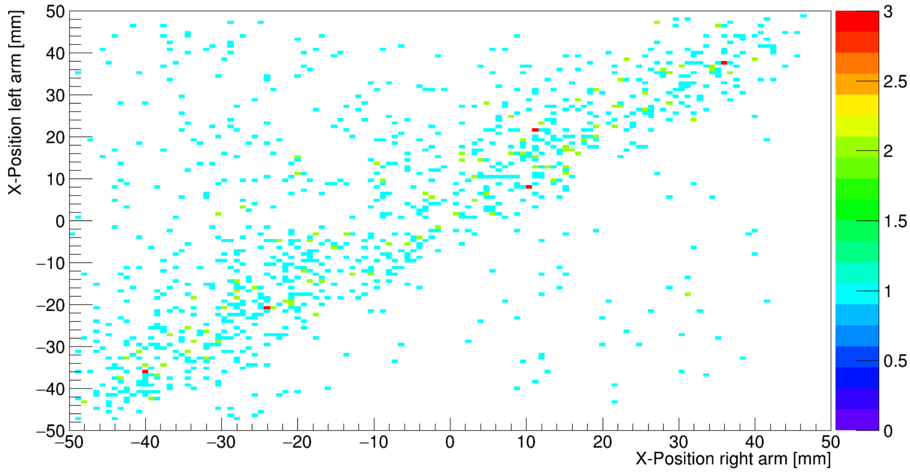

Figure 5.8: X-positions of the left arm against the right arm. At the diagonal a sharp edge can be seen, positioned at 84°. The intensity is smeared out to lower angles. This distribution is due to the kinematic of the (p,2p) reaction. Lower angles come from reactions with a higher excitation energy transferred to the nucleus. The result is in good agreement with Fig. 2.4.

determined. In addition background from the reactions with the C-atoms in the target has to be taken into account.

This data then allows for the extraction of the missing mass of the reaction giving the possibility to analyse excitation levels, and in the future, fission barrier heights of nuclei. As this goes far beyond the scope of this thesis, this work is done by S. Reichert working in the same group for his PhD thesis.

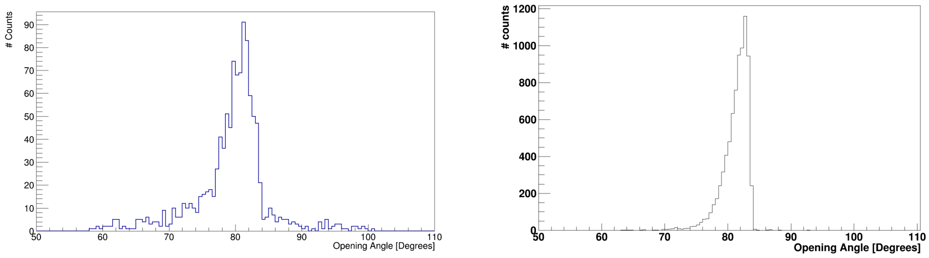

Figure 5.9: Distribution of the opening angle between the two protons.Experimental data is shown on the left, while the results from simulation are shown on the right side. The structure typical for the (p,2p) reaction is clearly visible. Lower angles are equivalent to higher exitation energies of the nucleus. The very low background is coming from other reactions, which can not be distinguished from (p,2p) reactions using the ΔE-E detector.

5.4 Efficiency

The detection efficiency for protons is an important quantity for the system, since it is needed to calculate the reaction cross sections from the measured data. To get a value for this, it is first necessary to identify protons with the tracker. As there are three detector layers in each arm, the efficiency of individual layers could be determined by a coincidence method. This has been done in two ways. For the third detector layer, protons have been identified in the first two layers and a tracking condition to the target area is required, since all protons hitting the third detector layer will also have passed through this two layers. The condition, that those particles should have hit the 3rd detector layer also within the acceptance is rather strong. The other way of identification, used for the first and second layer, was to use a track in one detector arm pointing to the target, which corresponds to a reaction in the target, and impose the detection of a nitrogen nucleus in the ΔE-E detector. One then looks for a proton in the third layer of the other telescope. This proton must have passed also Layer 1 and 2 in the second arm.

If an event fulfills this identification criteria, all ADC values above electronics threshold of the detector who's efficiency is to be determined are stored. (see Fig. 5.10 for a typical ADC spectrum without proton identification, compared to one with proton identification cut in the other detectors) The number of signals above the proton threshold (60 ADC channels for layers 1 and 2 and 120 ADC channels for layer 3) is then compared to the number of protons expected, thereby giving the efficiency of the detector. The results can be seen in table 5.2

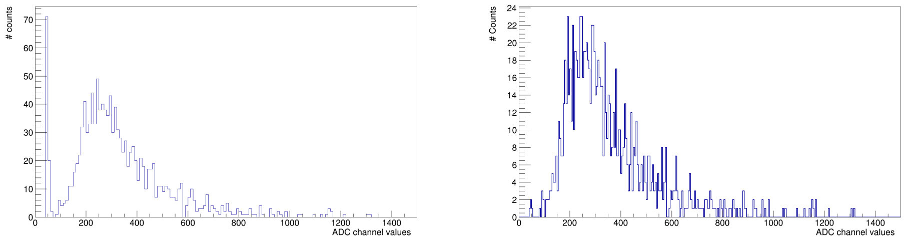

Figure 5.10: ADC spectra without (left) and with (right) proton identification. The typical structures of the proton spectra are well visible. Influence of the proton identification can be seen. Pictures show detector $L2_{xL}$, a detector typical for the first and second layer.

Detector	ϵ_A [%]	ϵ_{corr} [%]
$L1_{xL}$	99.78	99.78
$L1_{xR}$	97.86	97.86
$L2_{xL}$	99.85	99.85
$L2_{xR}$	99.71	99.71
$L3_{yL}$	83.59	~ 100
$L3_{yR}$	71.46	~ 100

Table 5.2: Detection probabilities for protons ϵ_A and detection efficiencies ϵ_{corr} corrected for geometric acceptance. The L3 detectors geometric uncertainty is not known precisely, therefore the calculated values for the L3 detectors have an uncertainty which makes their efficiency compatible with 100% $\pm$ 3%. Additionally, the detector $L3_{yR}$ had one defect APV, leading to a dead area of a sixth of the detector space. The correction for this dead area leads to an even higher uncertainty for this value.

For the third layer, this is not sufficient, it is necessary to correct for geometric acceptance. The third layer detectors cover less solid angle than the other detector layers. This allows to use the third layer to determine detection probabilities in the other two detector layers without having to correct for geometric efficiency, but also means that a geometric correction has to be done for the third layer.

The gap between the two wafers of the second layer does not have to be corrected for, because the third layer has an inactive area in the middle that is, d$\sim$2.4 mm wide, and roughly twice as big as the insensitive gap between the two wafers of layer 2. (The layout of the silicon detectors is shown in the appendix)

Corrections for geometrical acceptance are done in x-direction by cutting on events that hit the second layer detector in regions were they will no longer hit the third layer detector, the resulting value is ϵ_A of the third layer. Since this is not possible for the y direction, a calculation had to be performed for the geometric acceptance, leading to the result that the third layer covers only 83.5% of the dimensions of the second layer, in y-direction. This agrees well with the results shown in table 5.2. The slight fluctuation is expected for the third layer, since the geometrical coverage is not exact, due to uncertainties in positioning of the detectors as can be seen in Fig. 5.11. Overall, the system has a high corrected detection probability, calculated from table 5.2 to be 97.2 % for the detection of both protons from a (p,2p) reaction within the geometrical acceptance.

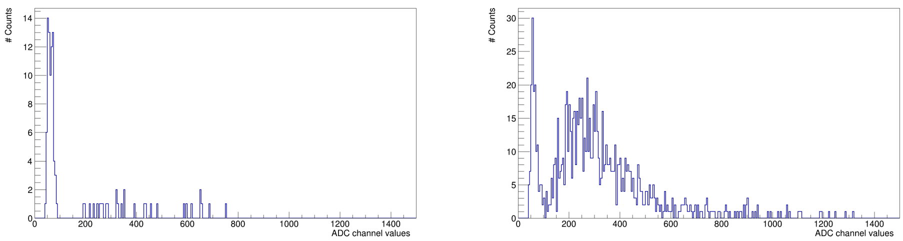

Figure 5.11: ADC spectrum for events cut away by the geometric cut for the third layer detectors (left), and ADC spectrum for the third layer detectors after the cut (right). The uncertainty in the geometrical cut is well visible, as well as the influence of the smaller solid angle coverage of the third layer. Several events with high ADC values have been cut away by the geometrical cut. This are most likely protons which did undergo angular straggling in the area of the second layer excluded by the cut, and thereby were scattered back to hit the third layer.

Chapter 6

Summary and outlook

A silicon detector system for tracking of protons in the (p,2p) reaction has been developed and tested. A low electronics noise level achieved for the system allowed for efficient detection of protons in thin (23 mg/cm^2) silicon wafers. The silicon tracker system has been combined with a gas drift chamber and arrays of plastic scintillators, allowing to measure the full four-momenta of the protons.

A simulation of the silicon detector system has been performed using Geant4. Resolution of the system and influence of angular straggling have been computed. Correlations between the telescope arms have been analysed in perspective of the Q-value determination of the (p,2p) reaction.

An experiment has been performed at the HIMAC facility in Japan, using a ^{16}O beam at 290 MeV/u with several targets. It was possible to separate protons from noise and identify particle tracks. Correlations expected from the simulation could be extracted from the data. Experimental resolutions nicely fit the predictions from full Geant4 simulation. The achieved resolution and measured opening angles are precise enough for a reconstruction of the Q-value exact within 1 MeV (assuming an uncertainty in the ToF measurement of 250 ps in sigma) to study spectroscopic factors in ^{16}O with the (p,2p) reaction.

The silicon detector system fulfils the recommended specifications excellently. It allows for a precise measurement of the opening angles. Also a high trigger rate is possible for the silicon tracker system, preventing a bottleneck in this part of the full detector system. Possible problems could arise from a worse then expected resolution of the drift chamber and an overall high dead time of the system, resulting in a limited maximum trigger rate. This should not be a problem for experiments done with exotic nuclei, since low trigger rates are expected for those.

The system is planned to be used together with the SAMURAI detector at the RIBF to measure fission barrier heights and daughter nuclei distributions for neutron rich, heavy nuclei. The motivation behind it being, that no experimental data exists for this quantities in the region close to the island of stability, while theoretical predictions for fission barrier heights show a huge diversion for this nuclei, depending on the model used. [4]

The SAMURAI detector will be used for identifying the heavy ions after the (p,2p) reaction has taken place. It is a dipole magnet with a bending power of 7 Tm and is combined with drift chambers and energy detectors to determine momentum, magnetic rigidity, charge and the energy of particles. [36] Combined with the described detector system this allows for a complete analysis of fission induced by a (p,2p) reaction. Using this detector systems, fission barrier heights and fission fragment distributions can be analysed for a variety of different ions.

6.1 Further improvements of the setup

Two major limitations for this type of experiment exist, which may put constraints on further experiments. A low rate of incoming exotic nuclei is expected. To increase the reaction rate, angular coverage of the system could be increased. One possibility would be to construct a ring of detectors around the beam line, all positioned at an angle of 42° relative to the beam axis. This would greatly enhance the acceptance. A second method is to use thick LH2 targets to increase the total luminosity. This would have the downside of increased scattering in the target, putting constraints on measurement precision.

6.1.1 Improvement of the Si-Wafers

To improve the resolution of the silicon tracker a lower thickness for the used silicon wafers is possible. Thinner silicon wafers also mean a lower energy deposition for the protons passing through them. This makes separation between protons and background ever more difficult the thinner the detectors get, thereby reducing the rate of detected (p,2p) reactions. Assuming that thinner detectors can be obtained, it is to decide which thickness would give the best compromise between resolution and detection efficiency. From Geant4 simulation, as described in chapter 2, with detector thicknesses ranging from 50 μm to 320 μm efficiency and detector resolution have been determined. It is worth noting, that the resolution achievable for the vertex x position with silicon strip detectors with a 100 μm strip pitch is not limited by the granularity but by scattering of particles in the target and the detector materials. Smaller strip pitches have therefore not been simulated.

d [μm]	rel. Eff. (T_{sim}=30 keV)	rel. Eff.(T_{sim}=10 keV)	Δ[μm]
320	1	1	612
200	0.9816	0.9823	499
100	0.9692	0.9574	400
75	0.9631	0.9468	318
50	0.8584	0.9344	306

Table 6.1: The efficiency normalised to the efficiency of a 320 μm thick detector, for detection thresholds of T_{sim}=30 keV and T_{sim}=10 keV, and the resolution of the vertex x position in FWHM are listed for different detector thicknesses. Details are described in the text.

Simulations have been performed assuming a fibre target, to allow for a simple analysis of the resolution quality. All resolution values mentioned are values for the reconstruction of the x-position of the vertex in one fibre. Table 6.1 shows the simulated detector thickness, the achieved resolution and the efficiency normalized to the detection efficiency of a 320 μm thick wafer. Due to the high number of strips per layer, a threshold for particle-noise distinction of $T_{sim}>6\sigma$ has to be applied, which corresponds to about 30 keV. For comparison, also a threshold of $T_{sim}>2\sigma$ has been used.

The values from table 6.1 have been plotted. The result can be seen in Fig. 6.1. With the current target, a thickness smaller then 75 μm will not yield an improvement. Efficiencies also drop significantly for detector thicknesses below 75 μm.

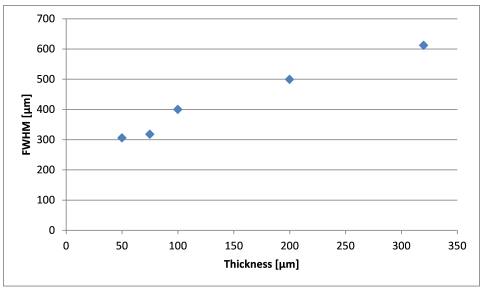

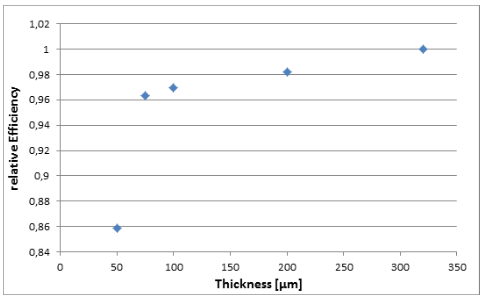

Figure 6.1: Resolution (left) and efficiency (right) plotted against detector thickness. The resolution is the FWHM of the vertex reconstruction of the x value using a 150 μm thick polypropylene target. The efficiency has been normalised to the efficiency of a 320 μm thick detector. The resolution plot shows a plateau at 300 μm. This suggests, that detectors below a thickness of around 75 μm would not yield improvements with the current target. The efficiency plot also shows a sharp drop around the d=75 μm mark.

6.1.2 The tagged fibre approach

Another possibility for improving the detector resolution would be to use a "tagged fibre" approach. A target consisting of many thin, separated fibres, comparable to the fibre target used at the experiment at HIMAC, would be used. The full detector system would be used to identify the fibre from which the protons originate, giving a vertex information in x and z accurate to the diameter of the fibre. This would allow for a determination of the angle, using only the first detector layer, eliminating the problems of angular straggling. This procedure has been performed in the before mentioned Geant4 simulation, allowing for a comparison between the true opening angles of the proton tracks, and the opening angles reconstructed with the full tracking and the tagged fibre approach. The comparison is shwon in Fig. 6.2. The improvement in the angle determination due to the tagged fibre approach can be clearly seen. The resolution is improved by a factor of two compared with the full tracking (5.4 mrad FWHM for the tagged fibre compared to 9.8 mrad for the full tracking).

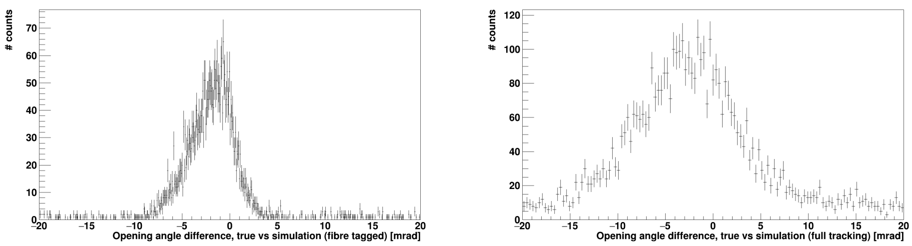

Figure 6.2: On the left, the difference between the true opening angle and the opening angle between the two protons determined by the tagged fibre approach can be seen. On the right the true opening angle and the opening angle between the two protons determined by the full tracking is shown for the same target. The tagged fibre approach yields a far better resolution. Assuming sufficient rates, the tagged fibre approach is superior to the conventional tracking method using unstructured targets.

A problem with this method would be the low target density due to the thin, spatially separated fibres. A combination of both concepts would be the ideal solution. While the fibres tag the high resolution vertex, a two layer tracking system just selects the corresponding fibre. This is similar to the concept used in the current experiment. As the results presented here show, a doubling of the fibre density is possible. Nevertheless this would introduce the need for a long target construction to yield sufficient rates for exotic ion beams. This could pose a constraint on the system, since a target covering to much of the beam axis could not fully be covered by the detectors. Overall, the density for this kind of target is limited by the distance between the fibres.

6.1.3 The active fibre method

The problem of fibre density could be circumvented by using an active fibre target, consisting of thin plastic scintillator fibres coupled to photomultipliers. This would allow for a fibre identification without the need for a full tracking of the protons in all dimensions. Horizontally close patched fibres can be used for the tagged fibre approach. In this approach the minimum distance between two fibres is only limited by the mechanical structure needed for precise positioning of the fibres. A remaining question concerns the optimal thickness of the fibres. For this, simulation has been performed for different thicknesses, and the opening angle resolutions achieved with the tagged fibre approach have been compared. The difference between 100 μm thick fibres and 200 μm thick fibres is 0.42 mrad in FWHM, or 7% of the FWHM for the 200 μm thick fibre, so even thicker fibres could be considered.

In conclusion, the silicon tracker system described here fulfils all expectations concerning noise levels, trigger rates and position resolution excellently, allowing for an optimal use of the system in future experiments. Additionally the system can be adapted to run optimal with low reaction rates (by using a ring of silicon detector in each layer instead of just one detector per layer and arm), or be optimized for precision determination of the (p,2p) kinematics by using the tagged fibre approach described here. Altogether the system is perfectly suited to be used in experiments set on determining the fission barrier heights of ions using the (p,2p) reaction, be it for very exotic, low rate beams, or in the exact measurement of barrier heights for more intense ion beams.

Bibliography

[1] BUSSO, M. ; GALLINO, R. ; WASSERBURG, G. J.: Nucleosynthesis in Asymptotic Giant Branch Stars: Relevance for Galactic Enrichment and Solar System Formation. In: *Annual Review of Astronomy and Astrophysics* 37 (1999), Nr. 1, 239-309. http://dx.doi.org/10.1146/annurev.astro.37.1.239. – DOI 10.1146/annurev.astro.37.1.239

[2] ARNOULD, M. ; GORIELY, S. ; TAKAHASHI, K.: The r-process of stellar nucleosynthesis: Astrophysics and nuclear physics achievements and mysteries. In: *Physics Reports* 450 (2007), Nr. 4-6, 97 - 213. http://dx.doi.org/http://dx.doi.org/10.1016/j.physrep.2007.06.002. – DOI http://dx.doi.org/10.1016/j.physrep.2007.06.002. – ISSN 0370–1573

[3] BUCHMANN, L. ; COMYN, M. ; THOMSON, J. ; GORIELY, S. ; DEMETRIOU, P. ; JANKA, H.-Th. ; PEARSON, J.M. ; SAMYN, M.: Nuclei in the Cosmos VIII The r-process nucleosynthesis: a continued challenge for nuclear physics and astrophysics. In: *Nuclear Physics A* 758 (2005), 587 - 594. http://dx.doi.org/http://dx.doi.org/10.1016/j.nuclphysa.2005.05.107. – DOI http://dx.doi.org/10.1016/j.nuclphysa.2005.05.107. – ISSN 0375–9474

[4] MAMDOUH, A. ; PEARSON, J.M. ; RAYET, M. ; TONDEUR, F.: Fission barriers of neutron-rich and superheavy nuclei calculated with the ETFSI method. In: *Nuclear Physics A* 679 (2001), Nr. 3, 337 - 358. http://dx.doi.org/http://dx.doi.org/10.1016/S0375-9474(00)00358-4. – DOI http://dx.doi.org/10.1016/S0375–9474(00)00358–4. – ISSN 0375–9474

[5] MEITNER, L. ; FRISCH, O.R.: The Mechanism of Nuclear Fission. In: *Nature* 143 (1939), March, 471–472. http://dx.doi.org/doi:10.1038/143471a0. – DOI doi:10.1038/143471a0

[6] BOHR, Niels ; WHEELER, John A.: The Mechanism of Nuclear Fission. In: *Phys. Rev.* 56 (1939), Sep, 426–450. http://dx.doi.org/10.1103/PhysRev.56.426. – DOI 10.1103/PhysRev.56.426

[7] MÖLLER, Peter ; SIERK, Arnold J. ; ICHIKAWA, Takatoshi ; IWAMOTO, Akira ; BENGTSSON, Ragnar ; UHRENHOLT, Henrik ; ÅBERG, Sven: Heavy-element fission barriers. In: *Phys. Rev. C* 79 (2009), Jun, 064304. http://dx.doi.org/10.1103/PhysRevC.79.064304. – DOI 10.1103/PhysRevC.79.064304

[8] POVH, B. ; RITH, K. ; SCHOLZ, C. ; ZETSCHE, F.: Teilchen und Kerne. (2009), S. 33, 278

[9] SPECHT, Hans J.: Nuclear fission. In: *Rev. Mod. Phys.* 46 (1974), Oct, 773–787. http://dx.doi.org/10.1103/RevModPhys.46.773. – DOI 10.1103/RevModPhys.46.773

[10] MOLLER, P. ; NIX, J.R. ; MYERS, W.D. ; SWIATECKI, W.J.: Nuclear Ground-State Masses and Deformations. In: *Atomic Data and Nuclear Data Tables* 59 (1995), Nr. 2, 185 - 381. http://dx.doi.org/http://dx.doi.org/10.1006/adnd.1995.1002. – DOI http://dx.doi.org/10.1006/adnd.1995.1002. – ISSN 0092–640X

[11] OGANESSIAN, Yuri: Nuclei in the "Island of Stability" of Superheavy Elements. In: *Journal of Physics: Conference Series* 337 (2012), Nr. 1, 012005. http://stacks.iop.org/1742-6596/337/i=1/a=012005

[12] DÜLLMANN, Ch. E. ; SCHÄDEL, M. ; YAKUSHEV, A. ; TÜRLER, A. ; EBERHARDT, K. ; KRATZ, J. V. ; ACKERMANN, D. ; ANDERSSON, L.-L. ; BLOCK, M. ; BRÜCHLE, W. ; DVORAK, J. ; ESSEL, H. G. ; ELLISON, P. A. ; EVEN, J. ; GATES, J. M. ; GORSHKOV, A. ; GRAEGER, R. ; GREGORICH, K. E. ; HARTMANN, W. ; HERZBERG, R.-D. ; HESSBERGER, F. P. ; HILD, D. ; HÜBNER, A. ; JÄGER, E. ; KHUYAGBAATAR, J. ; KINDLER, B. ; KRIER, J. ; KURZ, N. ; LAHIRI, S. ; LIEBE, D. ; LOMMEL, B. ; MAITI, M. ; NITSCHE, H. ; OMTVEDT, J. P. ; PARR, E. ; RUDOLPH, D. ; RUNKE, J. ; SCHAUSTEN, B. ; SCHIMPF, E. ; SEMCHENKOV, A. ; STEINER, J. ; THÖRLE-POSPIECH, P. ; UUSITALO, J. ; WEGRZECKI, M. ; WIEHL, N.: Production and Decay of Element 114: High Cross Sections and the New Nucleus ^{277}Hs. In: *Phys. Rev. Lett.* 104 (2010), Jun, 252701. http://dx.doi.org/10.1103/PhysRevLett.104.252701. – DOI 10.1103/PhysRevLett.104.252701

[13] M. VESELSKY, A.N. Andreyev M. Huyse P. Van Duppen F. Renzi K.Nishio H. Makii I. Nishinaka S. Chiba G. Souliotis P. Fountas N. Vonta T.Grahn P.T. Greenlees J. Pakarinen P. Rahkila M. Venhart J. Kliman S.Hlavac V. Matousek L. Krupa I. Sivacek D. Klc M. Sedlak E. R. R. Raabe R. R. Raabe ; ACTAR TPC COLLABORATIONI the: (d,p)-transfer induced fission of heavy radioactive beams. In: *Proposal to the ISOLDE and Neutron Time-of-Flight Committee* 450 (2012), Nr. 4-6, 97 - 213

[14] JACOB, GERHARD ; MARIS, TH. A. J.: Quasi-Free Scattering and Nuclear Structure. In: *Rev. Mod. Phys.* 38 (1966), Jan, 121–142. http://dx.doi.org/10.1103/RevModPhys.38.121. – DOI 10.1103/RevModPhys.38.121

[15] AUMANN, T. ; BERTULANI, C. A. ; RYCKEBUSCH, J.: Quasifree (p,2p) and (p,pn) reactions with unstable nuclei. In: *Phys. Rev. C* 88 (2013), Dec, 064610. http://dx.doi.org/10.1103/PhysRevC.88.064610. – DOI 10.1103/PhysRevC.88.064610

[16] KERMAN, A.K ; MCMANUS, H ; THALER, R.M: The scattering of fast nucleons from nuclei. In: *Annals of Physics* 8 (1959), Nr. 4, 551 - 635. http://dx.doi.org/http://dx.doi.org/10.1016/0003-4916(59)90076-4. – DOI http://dx.doi.org/10.1016/0003–4916(59)90076–4. – ISSN 0003–4916

[17] CARETTO, A. A. ; FRIEDLANDER, G.: (p, pn) and (p, 2p) Reactions of Ce^{142} at Proton Energies from 0.4 to 3.0 Bev. In: *Phys. Rev.* 110 (1958), Jun, 1169–1173. http://dx.doi.org/10.1103/PhysRev.110.1169. – DOI 10.1103/PhysRev.110.1169

[18] HASSAN, A. A. ; LUKYANOV, S. M. ; KALPAKCHIEVA, R. ; SKOBELEV, N. K. ; PENIONZHKEVICH, Yu. E. ; DLOUHÝ, Z. ; RADNEV, S. ; POROSHIN, N. V.: Setup for fission and evaporation cross-section measurements in reactions induced by secondary beams. In: *Physics of Atomic Nuclei* 66 (2003), Nr. 9, 1659–1662. http://dx.doi.org/10.1134/1.1611578. – DOI 10.1134/1.1611578. – ISSN 1562–692X

[19] RIKEN: *Riken Nishina Center, User Information, Accelerator and BigRIPS*. http://www.nishina.riken.jp/RIBF/

[20] R.GELLER: New high intensity ion source with very low extraction voltage. In: *Appl. Phys. Lett.* 16 (1970), May, 401. http://dx.doi.org/10.1063/1.1653043. – DOI 10.1063/1.1653043

[21] RIKEN: *Riken Nishina Center, User Information, Intensity*. http://www.nishina.riken.jp/RIBF/BigRIPS/intensity.html

[22] JONES, Lawrence: *APV25-S1 User GuideVersion 2.2*. https://cds.cern.ch/record/1069892/files/cer-002725643.pdf

[23] BNL: *APV HIP Dead Time, Response to issues raised during the HFT CD-1 review on Nov. 12, 2009*. http://www4.rcf.bnl.gov/~nieuwhzs/CD-1_Response_APV_HIP_15Dec2009.pdf

[24] MICHEL, Jan ; BOHMER, Michael ; FROHLICH, Ingo ; KORCYL, Grzegorz ; MAIER, Ludwig ; PALKA, Marek ; STROTH, Joachim ; TRAXLER, Michael ; YUREVICH, Sergey: The HADES DAQ system: Trigger and readout board network. In: *IEEE Trans. Nucl. Sci.* 58 (2011), S. 1745–1750. http://dx.doi.org/10.1109/TNS.2011.2141150. – DOI 10.1109/TNS.2011.2141150

[25] BOHMER, M.: *Private communication*. 2016

[26] TRAXLER, M ; BAYER, E ; KAJETANOWICZ, M ; KORCYL, G ; MAIER, L ; MICHEL, J ; PALKA, M ; UGUR, C: A compact system for high precision time measurements (< 14 ps RMS) and integrated data acquisition for a large number of channels. In: *Journal of Instrumentation* 6 (2011), Nr. 12, C12004. `http://stacks.iop.org/1748-0221/6/i=12/a=C12004`

[27] GRZEGORZ KORCYL, Jan Michel Andreas Neiser Marek Palka Manuel Penschuck Pawel Strzempek Michael Traxler Cahit U. Ludwig Maier M. Ludwig Maier: *A Users Guide to the TRB3 and FPGA-TDC Based Platforms*. `http://trb.gsi.de/`

[28] JAN MICHEL, Michael Böhmer Grzegorz Korcyl Marek Palka Sergey Yurevich Michael T. Jörn Adamczewski-Musch: *A Users Guide to the HADES DAQ System*. `http://trb.gsi.de/`

[29] MAIER, L.: *Private communication*. 2016

[30] NODA, K. ; FURUKAWA, T. ; FUJIMOTO, T. ; HARA, Y. ; INANIWA, T. ; IWATA, Y. ; KATAGIRI, K. ; KANEMATSU, N. ; MIZUSHIMA, K. ; MIYOSHI, T. ; MORI, S. ; MURAKAMI, T. ; SANO, Y. ; SATO, S. ; SHIRAI, T. ; TAKADA, E. ; TAKEI, Y. ; YONAI, S.: Recent progress of {HIMAC} for sophisticated heavy-ion cancer radiotherapy. In: *Nuclear Instruments and Methods in Physics Research Section B: Beam Interactions with Materials and Atoms* 331 (2014), 6 - 9. `http://dx.doi.org/http://dx.doi.org/10.1016/j.nimb.2013.12.036`. – DOI http://dx.doi.org/10.1016/j.nimb.2013.12.036. – ISSN 0168–583X. – 11th European Conference on Accelerators in Applied Research and Technology

[31] BAUER, J ; SOMMERER, F ; MAIRANI, A ; UNHOLTZ, D ; FAROOK, R ; HANDRACK, J ; FREY, K ; MARCELOS, T ; TESSONNIER, T ; ECKER, S ; ACKERMANN, B ; ELLERBROCK, M ; DEBUS, J ; PARODI, K: Integration and evaluation of automated Monte Carlo simulations in the clinical practice of scanned proton and carbon ion beam therapy. In: *Physics in Medicine and Biology* 59 (2014), Nr. 16, 4635. `http://stacks.iop.org/0031-9155/59/i=16/a=4635`

[32] A. KITAGAWA, M. Muramatsu Y. Sakamoto T. Sakuma N. Sasaki T. Sasano W. Takasugi S. Biri A.G. D. T. Fujita F. T. Fujita: STATUS OF ION SOURCES AT HIMAC. In: *Proceedings of ECRIS2010, Grenoble, France* MOCOBK03 (2010). `https://accelconf.web.cern.ch/accelconf/ECRIS2010/papers/mocobk03.pdf`

[33] NRIS: *NRIS, Department of Accelerator and Medical physics*. `http://www.nirs.go.jp/ENG/core/ace/index.html`

[34] WEBBER, W. R. ; KISH, J. C. ; SCHRIER, D. A.: Individual isotopic fragmentation cross sections of relativistic nuclei in hydrogen, helium, and carbon targets. In: *Phys. Rev. C* 41 (1990), Feb, 547–565. `http://dx.doi.org/10.1103/PhysRevC.41.547`. – DOI 10.1103/PhysRevC.41.547

[35] WEBBER, W. R. ; KISH, J. C. ; SCHRIER, D. A.: Individual charge changing fragmentation cross sections of relativistic nuclei in hydrogen, helium, and carbon targets. In: *Phys. Rev. C* 41 (1990), Feb, 533–546. `http://dx.doi.org/10.1103/PhysRevC.41.533`. – DOI 10.1103/PhysRevC.41.533

[36] KOBAYASHI, T. ; CHIGA, N. ; ISOBE, T. ; KONDO, Y. ; KUBO, T. ; KUSAKA, K. ; MOTOBAYASHI, T. ; NAKAMURA, T. ; OHNISHI, J. ; OKUNO, H. ; OTSU, H. ; SAKO, T. ; SATO, H. ; SHIMIZU, Y. ; SEKIGUCHI, K. ; TAKAHASHI, K. ; TANAKA, R. ; YONEDA, K.: {SAMURAI} spectrometer for {RI} beam experiments. In: *Nuclear Instruments and Methods in Physics Research Section B: Beam Interactions with Materials and Atoms* 317, Part B (2013), 294 - 304. `http://dx.doi.org/http://dx.doi.org/10.1016/j.nimb.2013.05.089`. – DOI http://dx.doi.org/10.1016/j.nimb.2013.05.089. – ISSN 0168–583X. – {XVIth} International Conference on ElectroMagnetic Isotope Separators and Techniques Related to their Applications, December, 2012 at Matsue, Japan

<Main Sensor Type A>

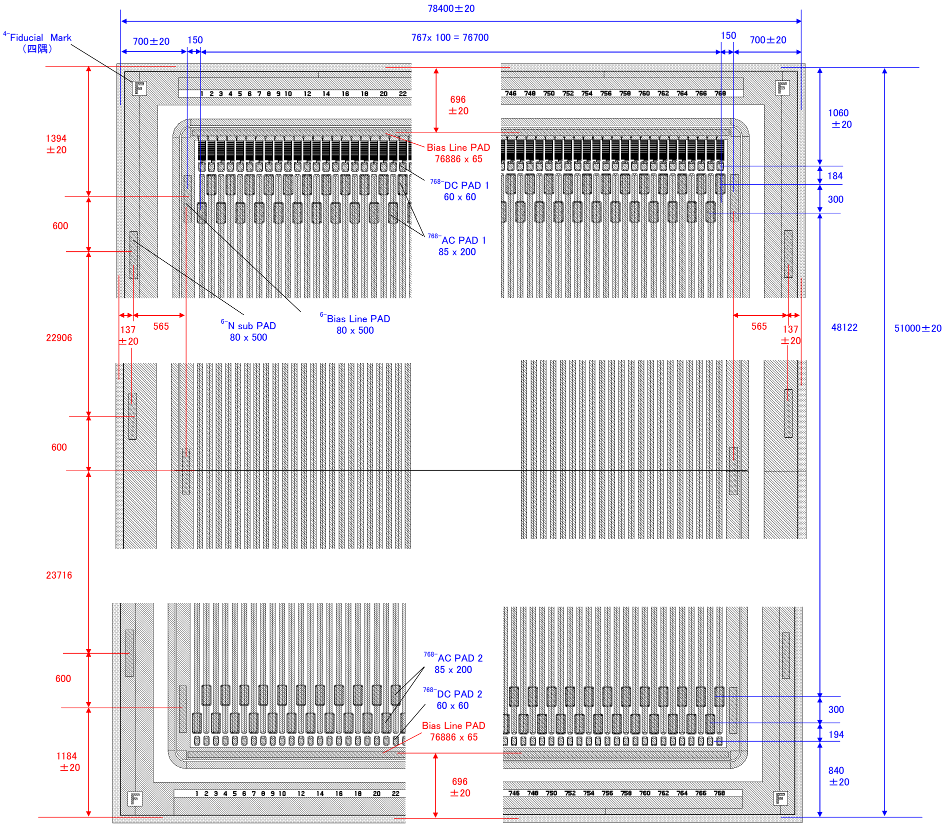

c		. .					UNIT 単位	μm	SCALE 尺度	／	TITLE 名称	RI ビーム実験用 SSD　Main-TypeA	
b		. .											
a		. .					PROJ 三角法				DWG NO 図番	K30-F10724-02	REV 改訂 A
	FIRST ISSUE　初発行	2015. 5. 26											
MARK 記号	CONTENTS 記　事	DATE 年月日	APPR 承認	CHCK 検図	DESN 設計	DRAW 製図	REF 備考				HAMAMATSU PHOTONICS K.K. 浜松ホトニクス株式会社		

様式ＫＸＸ－５２－３　Ａ

＜Main Sensor Type B＞

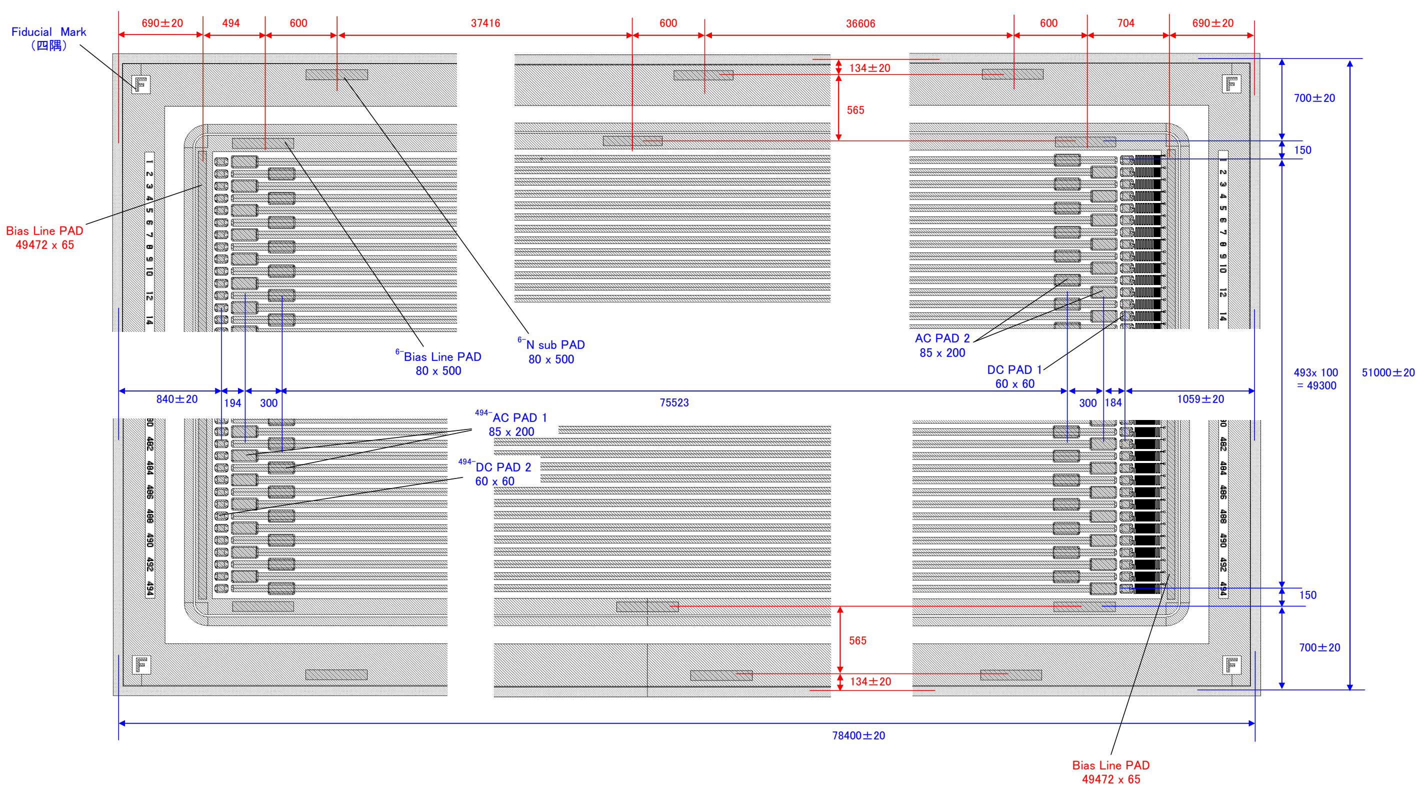

c		. .					UNIT 単位	μm	SCALE 尺度	／	TITLE 名称	RI ビーム実験用 SSD Main-TypeB
b		. .										
a		. .					PROJ 三角法				DWG NO 図番	K30-F10724-03 REV 改訂 A
	FIRST ISSUE 初発行	2015. 5. 26										
MARK 記号	CONTENTS 記 事	DATE 年月日	APPR 承認	CHCK 検図	DESN 設計	DRAW 製図	REF 備考					HAMAMATSU PHOTONICS K.K. 浜松ホトニクス株式会社